Geophys. J. Int. (2002) **149,** 679–697

Three-dimensional numerical modelling and inversion of magnetometric resistivity data

Jiuping Chen, Eldad Haber and Douglas W. Oldenburg

Department of Earth and Ocean Science, University of British Columbia, Vancouver, British Columbia, V6T 1Z4, *Canada. E-mail: jchen@geop.ubc.ca*

Accepted 2001 December 14. Received 2001 November 15; in original form 2001 June 26

SUMMARY

We develop an algorithm to model the magnetometric resistivity (MMR) response over an arbitrary 3-D conductivity structure and a method for inverting surface MMR data to recover a 3-D distribution of conductivity contrast. In the forward modelling algorithm, the second-order partial differential equations for the scalar and vector potentials are discretized on a staggered-grid using the finite-volume technique. The resulting matrix equations are consequently solved using the bi-conjugate gradient stabilizing (BiCGSTAB), combined with symmetric successive over relaxation (SSOR) pre-conditioning. In the inversion method, we discretize the 3-D model into a large number of rectangular cells of constant conductivity, and the final solution is obtained by minimizing a global objective function composed of the model objective function and data misfit. Since 1-D conductivity variations are an annihilator for surface MMR data, the model objective function is formulated in terms of relative conductivity with respect to a reference model. A depth weighting that counteracts the natural decay of the kernels is shown to be essential in typical problems. All minimizations are carried out with the Gauss–Newton algorithm and model perturbations at each iteration are obtained by a conjugate gradient least-squares method (CGLS), in which only the sensitivity matrix and its transpose multiplying a vector are required. For surface MMR data, there are two forms of fundamental ambiguities for recovery of the conductivity. First, magnetic field data can determine electrical conductivity only to within a multiplicative constant. Thus for a body buried in a uniform host medium, we can find only the relative conductivity contrast, not the absolute values. The choice of a constant reference model has no effect on the reconstruction of the relative conductivity. The second ambiguity arises from the fact that surface MMR cannot distinguish between a homogeneous half-space and a 1-D conductive medium. For a 3-D body in a 1-D layered medium, it is still difficult to obtain information concerning the general background 1-D medium, if sources and receivers are at the surface. Overall, the surface MMR technique is useful so long as significant current flows through the body. This happens when the overburden is thin and moderately conductive (less than 10 times the conductivity of the underlying basement) and if the current sources are placed so there is good coupling with the body. Our inversion method is applied to synthetic examples and to a field data set. The low-resolution image obtained from using traditional MMR data, involving one source and one magnetic component, illustrates the need for acquiring data from multiple sources if 3-D structure of complex geometries are sought.

Key words: 3-D, forward modelling, inversion, magnetometric resistivity, mineral exploration, MMR.

1 INTRODUCTION

The magnetometric resistivity (MMR) method involves the measurement of magnetic fields associated with artificially created, non-inductive (DC or pseudo-DC) current flow input to the earth through two electrodes. Historically, for a surface MMR survey, the wire connecting the two current electrodes is typically laid in a horse-shoe array and measurements are made somewhere in between the electrode spread. The observations are then reduced by subtracting the theoretical magnetic field arising from current flow in the wire and also the field owing to current flow in a uniform half-space or 1-D layered earth. The latter is often referred to as a 'normal' magnetic field. After the reduction, the remainders are expressed as a percentage of the normal field at either the centre of the study

area, or the centre of the relevant profile. Information concerning the conductivity distribution beneath the surface is then extracted with the aid of some data processing techniques. For down-hole or marine MMR measurements, data processing is slightly different since the receivers are located in bore-holes or on the seafloor. Edwards & Nabighian (1991) gives a thorough description of the theoretical work, modern implementation and case studies concerning the MMR method. In this paper, though, we do not explicitly connect the words MMR with a specific layout of current electrodes. The work here is valid for all locations of current sources and receivers. We will, however, use the typical horseshoe layout as an example, since it serves as a good illustration and also is needed for our field data set.

MMR methods have advantages over conventional electrical resistivity methods. The MMR measurement has greater sensitivity to conductive targets beneath a moderately conductive overburden than does the DC-electrical method (Edwards & Nabighian 1991). For example, an overburden of conductivity 0.01 S m^{-1}, 30 m thick, will dramatically reduce the response from a conductive target located in a basement of 0.001 S m^{-1} for a DC-electrical survey; however, the corresponding MMR anomaly is only reduced by about 10 per cent, compared with that without the conductive overburden (see Fig. 9). Thus DC-electrical surveys are not useful in such areas where the weathered layer has a conductivity that is one or more orders of magnitude higher than the conductivity of the underlying rock, but MMR is a feasible method. In addition, MMR is only sensitive to the relative conductivity between the targets and their surroundings, not the absolute conductivity values. This makes MMR an attractive technique for detecting poorly conducting targets such as some zinc deposits (Bishop *et al.* 1997).

Despite these positive attributes, MMR is not a routinely used method in mineral exploration, although it was successfully applied by Edwards (1974) two decades ago. There are two principal difficulties. The first is that the MMR signal is generally low, and great care, and good instrumentation are required at the data acquisition phase. The second impediment is the complexity of the observations; the maps of individual components bear no simple relationship to the geometry of the conductors. Fig. 1 is a manifestation of this. A simple cubic body with side length of 400 m and conductivity 0.1 S m^{-1}, is located in a host of conductivity 0.001 S m^{-1}. The top depth of the cube is 80 m. The source and sink electrodes are located on the x-axis; each is 600 m from the origin of the coordinates. The three synthetic components of the anomalous magnetic field at the surface have totally different anomaly patterns; the y-component is positive above the target; the vertical component changes sign from the upper panel to the bottom, while the x-component shows an anomaly in all four quadrants. Except for the y-component, there is little compelling evidence to indicate a conductive body at depth, never mind trying to infer information directly concerning the conductivity contrast and buried depth.

Calculation of MMR responses over a conductive structure can be roughly grouped into three categories. The first is based on analytical derivations for simple structures. As summarized in Edwards *et al.* (1978), these structures include an anisotropic earth, vertical and dipping contacts, thin and thick dykes, and semi-cylindrical and hemispherical depressions, as well as α-media. Inayat-Hussein (1989) developed and used a Fourier series integral to compute the magnetic field of a direct current in a cylindrical-shaped conductor embedded in a resistive half-space beneath a conductive surface layer. The second method for forward modelling is based upon the modification of a numerical 'resistivity' method (Edwards & Nabighian 1991). This involves two steps. The first is to solve the Poisson equation for the electric potential by using the standard finite-element or finite-difference techniques. This is the same procedure implemented in the conventional DC-electrical forward problem. The second step is to calculate the magnetic field through the modified form of the Biot–Savart law in which magnetic field is explicitly expressed as a volume integral of a functional that is proportional to the cross-product of the gradient of the potential and the conductivity throughout the volume (Edwards *et al.* 1978). Pai & Edwards (1983), Acosta & Worthington (1983) and Yang & Tseng (1992) all followed this procedure to compute the MMR response over a 2-D conductivity model. More recently, Boggs *et al.* (1999) developed a finite-difference method for evaluating total field magnetometric resistivity (TFMMR) responses of 3-D structures. In their work, the magnetic field was evaluated in the Fourier domain. The third method for forward modelling is the surface integral equation method. For many simple problems, the gradient of the electrical conductivity vanishes everywhere except on the surfaces defining changes in conductivity. Consequently, the volume integral for the modified Biot–Savart law is reduced to a finite set of surface integrals. Gomez Trevino & Edwards (1979) derived a rapid algorithm for evaluating the three components of the magnetic field over a 2-D structure. Oppliger (1984) modelled the effect of 3-D topography, while Nabighian *et al.* (1984) and Cheesman & Edwards (1989) computed MMR anomalies associated with multiple finite plates of arbitrary conductance.

In this paper we perform forward modelling by using the method proposed by Haber (2000) except we use a finite-volume solution rather than the mixed finite elements. Effectively the MMR modelling can be regarded as a mixed subproblem of electrostatic and magnetostatic problems. One first solves an electrostatic problem for a scalar potential, and then solves a magnetostatic equation for the magnetic field. The first stage is therefore similar to the finite-difference modelling mentioned in the previous paragraph, but the second stage is different in that we obtain the magnetic field by solving a differential equation rather than by performing a volume integration.

In contrast to the forward modelling, inversion techniques of MMR data are less developed. Type curves (Howland-Rose *et al.* 1980) are used to estimate qualitatively the source of some simple 2-D targets, and trial-and-error interpretation has been developed based upon the gravity–MMR relationship given by Szarka (1987). This relationship has been exploited with some success by using the standard 2-D gravity modelling suite for processing down-hole MMR data (Asten 1988). As recognized by Bishop *et al.* (1997), however, standard gravity programs, which generally assume flat surface traverses, may be not suited to surveys down deviating drill holes. Consequently, the results have to be best-fitted by hand on to geological cross-sections. A full 3-D interpretation program is expected to be able to overcome such difficulties and to extract more useful information concerning the conductivity from the measured data.

In this paper, we first develop a numerical algorithm to model the MMR responses of an arbitrary 3-D conductivity structure. The governing second-order differential equations for scalar and vector potentials are split into two first-order equations, and then discretized on a staggered grid by using a finite-volume method (Haber & Ascher 2001). This discretization scheme is second-order accurate and allows us to cope with highly discontinuous conductivity and permeability. Scalar potentials are defined at the centres of grid cells, while vector potentials are located on the faces. Conductivity values at cell faces are harmonically averaged, while permeability values at edges are arithmetically averaged. The resulting

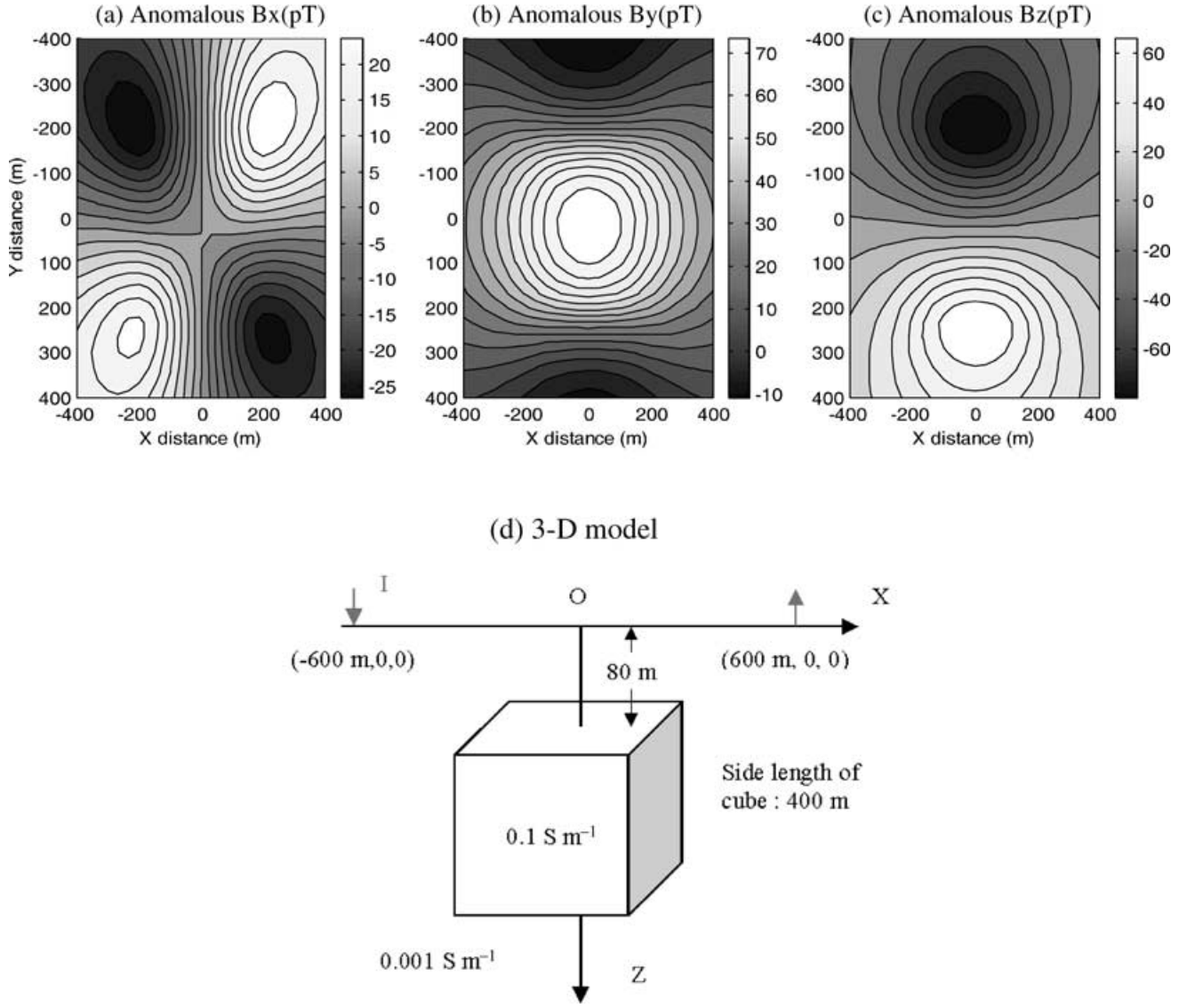

Figure 1. Anomalous magnetic fields at the surface produced by a 400 × 400 × 400 m^3 cube (d) with conductivity of 0.1 S m^{-1} and a top depth of 80 m, embedded in a host of 0.001 S m^{-1}. The source and sink electrodes are located at the *x*-axis, 600 m each from the origin of the coordinates: (a) *x*-component; (b) *y*-component; (c) *z*-component. The magnitudes are in picoTesla (pT).

matrix equations are solved using the biconjugate gradient stabilized (BiCGSTAB) method, combined with a symmetric successive over-relaxation (SSOR) pre-conditioning. Once the two potentials are computed, the magnetic field (and electric field, if required) can be obtained anywhere by applying the discrete matrix for the curl operator to the vector potentials. This numerical algorithm is verified by comparison with the analytic solutions over a vertical contact and a hemispherical depression. We also discuss the relationship between the MMR anomaly and the conductivity distribution; this helps us to define the 'model' parameter in our inversion algorithm. The inverse problem for MMR data is formulated as an optimization problem in which we minimize a model objective function subject to the constraints that the data misfit is achieved to some level. Our model objective function has the flexibility to incorporate extra information, and a Gauss–Newton iterative method is used to obtain the model perturbation at each iteration. The regularization parameter that controls the balance between the model norm and misfit is determined through a cooling process. At each iteration we must solve a large matrix system. We use a conjugate gradient least-squares (CGLS) method and hence the majority of computations involve multiplying a sensitivity matrix, or its transpose, by an arbitrary vector. This can be accomplished without explicitly calculating and storing the sensitivity matrix (Haber *et al.* 2000b).

The paper begins by formulating the finite-volume discretization for forward modelling of MMR response and then by formulating the inverse algorithm. Practical considerations pertaining to the inverse problems, such as how to define a depth weighting to counteract the natural decay of the kernels, how to choose a reference model, and which component data should be inverted will be discussed using synthetic data. We then invert a field data set over a known mineral deposit and conclude the paper with a discussion.

2 3-D MMR FORWARD MODELLING

2.1 Governing equations

In a typical MMR survey, an external current is impressed into the ground through a pair of current electrodes. The magnetic field

associated with the current flow in both the wire and ground can be measured by a magnetometer at the surface. For MMR modelling we can assume that the exciting source is a direct current (DC). This means that the solution for general Maxwell equations in the frequency domain can be reduced to a steady-state problem (the frequency is zero), which can be written as

$$\nabla \times \mathbf{E} = 0, \tag{1a}$$

$$\nabla \times \mathbf{H} - \sigma \mathbf{E} = \mathbf{J}^{\mathbf{s}}, \tag{1b}$$

$$\nabla \cdot (\mu \mathbf{H}) = 0, \tag{1c}$$

where $\mathbf{E}$ is the electric field intensity in V m^{-1}, $\mathbf{H}$ is the magnetic field intensity in A m^{-1}, $\mathbf{J}^{\mathbf{s}}$ is the external electric current density in A m^{-2}, σ and μ are the electric conductivity and magnetic permeability, respectively. The constitutive relation $\mathbf{J} = \sigma \mathbf{E}$ has been incorporated into eq. (1b).

From eq. (1a), there exists a scalar electric potential ϕ, which allows us to write $\mathbf{E}$ as

$$\mathbf{E} = -\nabla \phi. \tag{2}$$

By taking the divergence of eq. (1b), we obtain the well-known DC equation

$$\nabla \cdot (\sigma \nabla \phi) = \nabla \cdot \mathbf{J}^{\mathbf{s}}. \tag{3}$$

With appropriate boundary conditions, this system of equations can be solved for ϕ. Once the potential ϕ is obtained, the magnetic field $\mathbf{H}$ can be computed by solving

$$\nabla \times \mathbf{H} = \mathbf{J}^{\mathbf{s}} - \sigma \nabla \phi = \mathbf{f}, \tag{4}$$

along with eq. (1c). In eq. (4), the scalar potential ϕ is on the right-hand side of eq. (4), and serves as a source term to produce the magnetic field. The source term $\mathbf{f}$ in eq. (4) should implicitly satisfy the compatibility condition $\nabla \cdot \mathbf{f} = 0$. Eqs (4) and (1c), along with boundary conditions, define a magnetostatic problem, and many numerical methods have been devoted to solving it (Jin 1993; Haber 2000). In order to solve for $\mathbf{H}$, we introduce a magnetic potential $\mathbf{A}$ such that

$$\mu \mathbf{H} = \nabla \times \mathbf{A}. \tag{5}$$

The introduction of the vector potential $\mathbf{A}$ makes eq. (1c) implicitly satisfied. Therefore, the system of equations for $\mathbf{A}$ can be written as

$$\nabla \times \mu^{-1} \nabla \times \mathbf{A} = \mathbf{f}, \tag{6a}$$

subject to appropriate boundary conditions. As encountered in other electromagnetic problems (Jin 1993), this equation does not have a unique solution owing to the null space of the curl operator, and therefore a gauge condition for $\mathbf{A}$ has to be imposed. We adopt the Coulomb gauge condition

$$\nabla \cdot \mathbf{A} = 0. \tag{6b}$$

The system of eqs (6) is in principle overdetermined, since we have four equations but only three unknowns. However, it is consistent since eq. (6b) exactly covers the null-space of the operator in eq. (6a). To ensure that the system remains positive definite, a stabilizer is added (Haber & Ascher 2001),

$$\nabla \times \mu^{-1} \nabla \times \mathbf{A} - \nabla \mu^{-1} \nabla \cdot \mathbf{A} = \mathbf{f}. \tag{7}$$

In order to obtain a second-order accurate method, even in the case of highly discontinuous conductivity and susceptibility, the variable

$$\psi = \mu^{-1} \nabla \cdot \mathbf{A}, \tag{8}$$

is introduced, and $\mathbf{H}$ is not eliminated from the system. The final system becomes

$$\nabla \times \mathbf{A} - \mu \mathbf{H} = 0, \tag{9a}$$

$$\nabla \cdot \mathbf{A} - \mu \psi = 0, \tag{9b}$$

$$\nabla \times \mathbf{H} - \nabla \psi = \mathbf{f}, \tag{9c}$$

which leads to a first-order, mixed formulation for the unknowns ($\mathbf{A}$, $\mathbf{H}$, ψ). Similarly, eq. (3) can also be decoupled into two first-order systems for the unknowns ($\mathbf{J}$, ϕ) as

$$\nabla \cdot \mathbf{J} = -\nabla \cdot \mathbf{J}^{\mathbf{s}}, \tag{10a}$$

$$\sigma^{-1} \mathbf{J} - \nabla \phi = 0. \tag{10b}$$

2.2 Discretization using finite volumes

The differential eqs (9) and (10) are discretized by a finite-volume method on a staggered grid (Haber *et al.* 2000a). An appealing characteristic of the finite-volume method is that discontinuous fields, such as the normal component of the electric field separating two regions of different conductivities, are handled by working with fluxes that are continuous. The study region is divided up by three orthogonal sets of constant coordinate surfaces, producing a matrix of rectangular cells. The 3-D volume must include the air since we want to solve for $\mathbf{A}$ and ϕ by using the same grid mesh. Each grid cell is assumed to have constant material properties (conductivity and permeability), but the property values can vary significantly from one cell to the next. In formulating a solution, care must be taken to consider the smoothness properties of the different unknown variables. An inappropriate location of variables can violate the conservation laws and implicit boundary conditions, and result in erroneous solutions. In our discretization scheme, $\mathbf{A}$ and $\mathbf{J}$ are chosen to be at the centres of cell faces, $\mathbf{H}$ at the centres of cell edges and ψ and ϕ are at cell centres, as shown in Fig. 2. By doing so, the continuity of normal $\mathbf{J}$, and tangential $\mathbf{H}$ across boundaries is preserved explicitly.

After having carefully defined the locations of variables, we can discretize eqs (9) and (10) in their weak forms. Detailed derivations are given in Haber & Ascher (2001). It is worthwhile pointing out

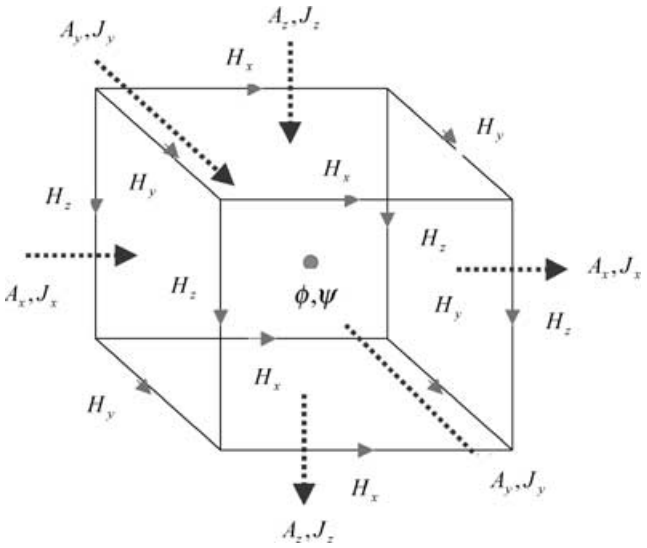

Figure 2. A grid cell showing the locations for each unknown variable. ϕ and ψ are at the centre of the cell; $\mathbf{A}$ and $\mathbf{J}$ are at the centre points of the faces, denoted by arrows with dashed tails; $\mathbf{H}$ is at the edges.

that firstly, this discretization is second-order accurate for both potentials and **H**. Secondly, we use harmonic averaging for values of σ at cell faces, and use arithmetic averaging for values of μ at cell edges. These choices arise naturally from the discretization of eqs (9) and (10), and are common to mixed methods. Thirdly, we can eliminate the auxiliary components of **J**, **H**, and ψ unambiguously by substituting eq. (10b) into eqs (10a), (9a) and (9b) into (9c), respectively. These algebraic eliminations correspond exactly to discretizing the second-order systems (3) and (7). Our resultant matrix system is

$$\begin{pmatrix} \nabla_h^{(e)} \times \mathbf{M}_e^{-1} \nabla_h^{(f)} \times & -\nabla_h \mathbf{M}_c^{-1} \nabla_h \cdot & \mathbf{S}\nabla_h \\ & 0 & \nabla_h \cdot \mathbf{S}\nabla_h \end{pmatrix} \begin{pmatrix} \mathbf{A} \\ \phi \end{pmatrix} = \begin{pmatrix} \mathbf{J}^s \\ \nabla_h \cdot \mathbf{J}^s \end{pmatrix}, \tag{11}$$

where the matrices $\nabla_h^{(e)}\times$ and $\nabla_h^{(f)}\times$ are assembled from the discretization of the **curl** operator, projecting from cell edges to faces and from faces to edges, respectively; matrices $\nabla_h\cdot$ and ∇_h correspond to the discretization of the **div** and **grad** operators. The material matrix $\mathbf{S}$ arises from the discretization of the conductivity, which is a harmonic averaging of values at cell faces. The matrices $\mathbf{M}_e$ and $\mathbf{M}_c$ result from an arithmetic averaging of the permeability at cell edges and the permeability at the cell centres, respectively. The superscript -1 represents the inverse of the matrix.

As pointed out by many researchers, such as Zhang *et al.* (1995) and Zhao & Yedlin (1996), boundary conditions are critical to accurately model the 3-D DC response using a finite-difference method. Mixed boundary conditions (Dey & Morrison 1979) are often used. In our implementation of the finite-volume method, we do not impose boundary conditions explicitly on the scalar potential ϕ, but normal components of **A** and **J**, and the tangential components of **H** are assumed to be zero. This requires that the outer boundaries must be far from the electrodes. In our following synthetic examples, the outer boundary in each direction is 2 km away from the origin, including the top boundary in the air.

2.3 Solving the system of equations

The large system of equations that result from a finite-volume approximation over a 3-D mesh can be solved using Krylov space iterative methods because a direct solution requires prohibitive amounts of memory and computation. The convergence of Krylov space methods depends on the condition number of the system matrix and on the clustering property of the eigenvalues. Convergence is greatly accelerated by applying an appropriate pre-conditioner. We use the biconjugate gradient stabilized method, or BiCGSTAB, proposed by Van der Vorst (1992), combined with a symmetric successive over relaxation (SSOR) for our problem.

Obviously, the system of eq. (11) is decoupled and it is not necessary to solve for **A** and ϕ simultaneously. We split them into two systems

$$\nabla_h \cdot \mathbf{S}\nabla_h \phi = \nabla_h \cdot \mathbf{J}^s, \tag{12}$$

and

$$\left(\nabla_h^{(e)} \times \mathbf{M}_e^{-1} \nabla_h^{(f)} \times -\nabla_h \mathbf{M}_c^{-1} \nabla_h \cdot\right) \mathbf{A} = \mathbf{J}^s - \mathbf{S}\nabla_h \phi. \tag{13}$$

The matrix eq. (12) is first solved, and we then substitute ϕ into eq. (13) and solve for **A**. A standard left and right pre-conditioning in the SSOR is applied to eqs (12) and (13), and then we use the BiCGSTAB subroutine coded by Barrett *et al.* (1994), to solve for ϕ and **A**.

After **A** and ϕ are obtained, the fields **H** (or **B**) and **E** (if required) can be computed elsewhere by matrix operations $\mathbf{M}_e^{-1}\nabla_h^{(f)} \times \mathbf{A}$ (or $\nabla_h^{(f)} \times \mathbf{A}$ for **B**) and $-\nabla_h\phi$. For convenience, we do not distinguish **H** and **B** from now on. Both are called as the magnetic field.

2.4 Computing magnetic data for MMR surveys

For a typical surface MMR set-up, a magnetic field sensor measures a component of the magnetic field that exists at any location. The magnetic field is caused by currents that flow in the Earth ($\mathbf{B}^g$) and in the wire ($\mathbf{B}^w$). Without consideration of various noise, the observed magnetic field $\mathbf{B}^{obs}$ can be denoted by

$$\mathbf{B}^{obs} = \mathbf{B}^w + \mathbf{B}^g. \tag{14}$$

From a numerical point of view, $\mathbf{B}^w$and $\mathbf{B}^g$ can be computed separately from the discretized matrix equations as shown in eq. (13). The right-hand side of eq. (13) represents the current source terms. The first term $\mathbf{J}^s$ corresponds to the current flow in the wire; the term $-\mathbf{S}\nabla_h\phi$ represents the current flow in the ground. This means that we have two options for calculating the magnetic field. Eq. (13) could be solved by including both current source terms. This is feasible but there are substantial discretization errors when fields are to be calculated close to the wire. This arises, because in the numerical implementation of a finite-volume solution, the current in the wire is effectively distributed over the face of a cell. A better procedure, and one used here, is to leave $\mathbf{J}^s$ out of eq. (13) and compute the magnetic field $\mathbf{B}^w$ analytically using the Biot–Savart law. The magnetic field $\mathbf{B}^w$ around a finite straight length of wire carrying current I can be obtained from the Biot–Savart law (Asten 1988) and is

$$\mathbf{B}^w = \frac{\mu I}{4\pi r}(\cos\alpha - \cos\beta)\,(\hat{\mathbf{I}} \times \hat{\mathbf{r}}), \tag{15}$$

where $\hat{\mathbf{I}}$ is a unit vector in the direction of current flow and $\hat{\mathbf{r}}$ is a unit vector perpendicular to the wire. α and β are the angles between the connecting line from the observation point to the ends of the wire and $\hat{\mathbf{I}}$. It is evident that $\mathbf{B}^w$ does not contain any information concerning the conductivity.

Following the MMR convention, the ground component $\mathbf{B}^g$ can also be split into two parts:

$$\mathbf{B}^g = \mathbf{B}^n + \mathbf{B}^a, \tag{16}$$

where $\mathbf{B}^n$ is the normal magnetic field associated with the current flow in a background media that may be a uniform half-space or 1-D earth; $\mathbf{B}^a$ is the anomalous magnetic field produced by the current variation with respect to the normal current. As shown in Edwards & Nabighian (1991), $\mathbf{B}^n$ at the surface is independent of the 1-D conductivity distribution beneath the earth, and is only related to the current amplitude and distance from the current. The vertical component of $\mathbf{B}^n$ is zero and the azimuthal $\mathbf{B}^n$, caused by a single impressed source electrode with a current of strength I over any 1-D earth, is given by

$$B_\phi^n = \frac{\mu I}{4\pi r}, \tag{17}$$

where r is the distance from the observation point to the electrode. This expression is independent of conductivity. It should be noted that eq. (17) only applies for surface MMR without any topography.

From the above, it follows that the only portion of useful signal from which electrical properties can be inferred is the anomalous magnetic field

$$\mathbf{B}^{\mathrm{a}} = \mathbf{B}^{\mathrm{obs}} - \mathbf{B}^{\mathrm{w}} - \mathbf{B}^{\mathrm{n}}. \tag{18}$$

Our numerical tests will focus on this quantity.

2.5 Verification of the forward modelling code

Edwards *et al.* (1978) present some analytical solutions for vertical and dipping contacts, thin and thick dikes, hemicylindrical and hemispherical depressions. We checked our code with two models: a vertical contact and an extremely conductive hemi-spherical depression. Analytical models were calculated directly from formulae given in Boggs (1999), which are slightly different from those given in Edwards *et al.* (1978). The discrepancies are attributed to typographical errors in the original reference (Boggs *et al.* 1999). Only formulae for the vertical component of the anomalous magnetic field, B_z^{a}, were available so we limited our comparison to that component.

As shown in Fig. 3(c), the vertical contact model consisted of two adjacent quarter-spaces with conductivities 0.01 and 0.001 S m^{-1}. The contact separating the two spaces is coincident with the *yoz* plane and the source and sink electrodes were located at the surface at the positions (0, −600, 0) m and (0, 600, 0) m, respectively. The analytical expression for B_z^{a} (Edwards & Nabighian 1991, p. 63), is not reproduced here. For numerical modelling, the 3-D model, 4 km × 4 km × 4 km, was unevenly discretized into 54 × 50 × 44 cells, including the 2 km air layer. A mesh size of 25 m was used to partition the centre region of the model and a larger mesh size for the rest of the model. The vertical component of the anomalous magnetic field over the area bounded by the coordinates −400 to 400 m in both *x* and *y* directions, is shown in Fig. 3(a). There is little visual difference between the analytical and computed magnetic field, so to compare, we plot the difference between them. Fig. 3(b) is the error map in pT.

In a second comparison (Fig. 4c) we modelled responses from a conductive (10 S m^{-1}) hemi-sphere of radius 200 m located at the origin of the coordinates. The host medium had a conductivity of 0.001 S m^{-1} and the current flow was from the source at (0, −600, 0) m to the sink at (0, 600, 0) m. The analytical vertical magnetic fields are given in (Edwards & Nabighian 1991, p. 71). We used the same mesh as in the contact case to discretize this hemisphere

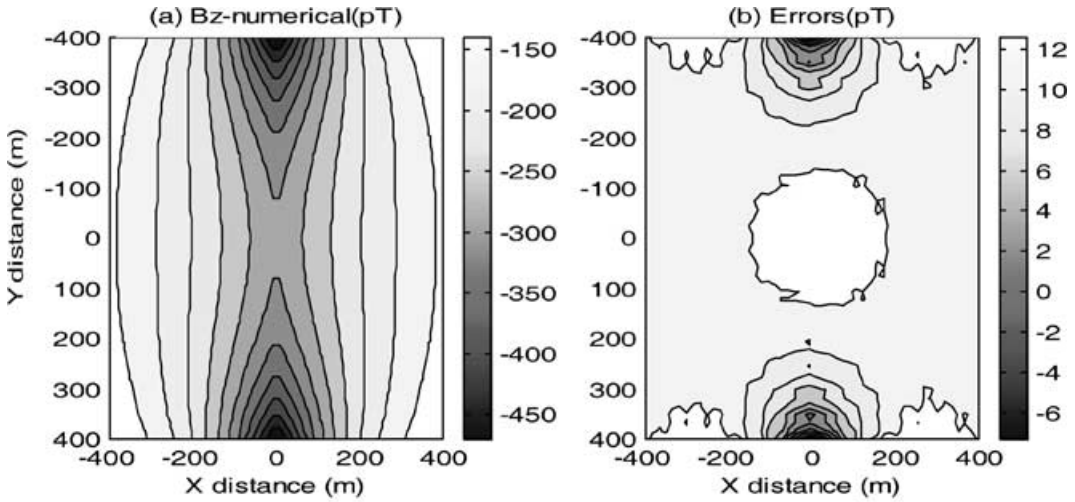

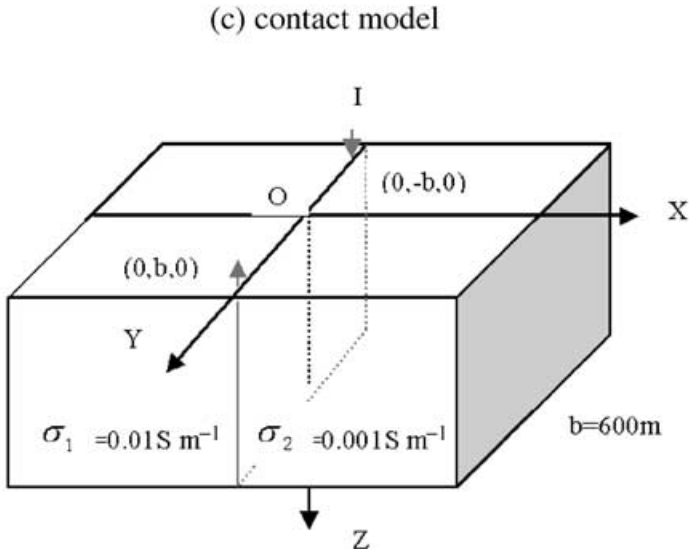

Figure 3. 3-D numerical vertical component of anomalous magnetic field (a) and its percentage error (b), compared with an analytical solution for a vertical contact model shown in (c). The source and sink electrodes, carrying 1.0 A, were located at (0, −600, 0) and (0, 600, 0) m, respectively.

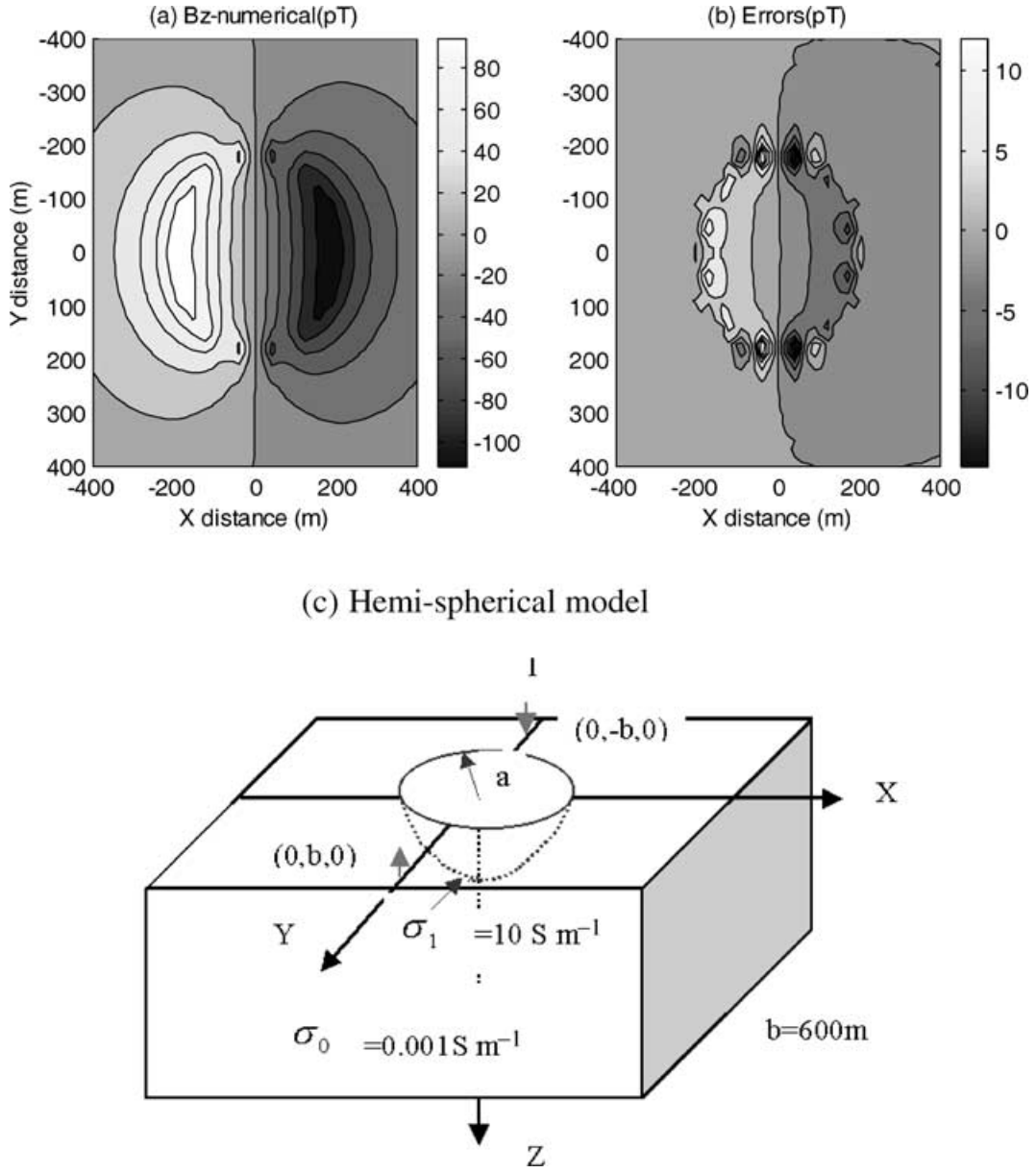

Figure 4. 3-D numerical vertical component of the anomalous magnetic field (a) and its percentage error (b), compared with the analytical solution for a hugely conductive hemi-sphere of radius 200 m shown in (c). The source and sink electrodes, carrying 1.0 A, were located at (0, −600, 0) and (0, 600, 0) m, respectively.

model. Results of the 3-D numerical modelling are presented in Fig. 4(a), and the difference error in the model is shown in Fig. 4(b). Larger errors (up to 14 pT) occur at the rim of the hemisphere, but errors in the rest of the study area are quite small. The error at the rim of the hemisphere is principally owing to the difficulty in trying to represent a spherical surface with cuboidal prisms. Rerunning the forward modelling after decreasing the cell size by a factor of 2 in the core area reduced the error to 8 pT.

2.6 Relationship between B and conductivity

Understanding the relationship between the magnetic field and the conductivity beneath the surface of the earth is important for inversion of MMR data. One may expect that different conductivity distributions will give rise to different magnetic fields and hence any change of the conductivity will be manifested in the observed data. This is true for the electric fields, and it allows us to recover absolute values of the conductivity from observed DC resistivity measurements, albeit there is the usual non-uniqueness associated with inverting a finite number of inaccurate data. The situation for MMR data is more complicated. We have already discussed one form of insensitivity, that is, the anomalous surface magnetic field is insensitive to 1-D variations in conductivity. In addition, identical magnetic fields arise from any two conductivities that differ only by a constant scaling factor.

To see this, consider a general conductivity model $\sigma_1(x, y, z)$ and compute potentials $\mathbf{A}$ from eq. (7) and ϕ from eq. (3). These two equations are uncoupled so ϕ can be determined solely from the latter equation. Now consider another conductivity model such that $\sigma_2(x, y, z) = \chi\sigma_1(x, y, z)$, where χ is a constant. From eq. (3), it is easy to see that $\phi_2 = \phi_1/\chi$, i.e. $\sigma_1\nabla\phi_1 = \sigma_2\nabla\phi_2$. So the source term $\mathbf{J}^s - \sigma\nabla\phi$ on the right-hand side of eq. (7) remains unchanged

for these two models. Since the left-hand side does not involve conductivity, the vector potential **A**, and hence the magnetic field **B**, are unchanged by this scaling. The same conclusion can also be obtained by working with the discretized eq. (11).

This clearly indicates that the magnetic field is not sensitive to the absolute conductivity. Thus if σ_0 is a constant reference background conductivity then the data are dependent upon a ratio of conductivities $\sigma(x, y, z)/\sigma_0$. The two analytic results presented earlier substantiate this. The analytical expressions of the anomalous magnetic field B_z^a are only related to conductivities through the reflection coefficients K_{21} for the vertical contact, and C_n for the hemispherical model. K_{21} and C_n are expressed as

$$K_{21} = \frac{1 - \sigma_2/\sigma_1}{1 + \sigma_2/\sigma_1}, \tag{19}$$

and

$$C_n = \frac{1 - \sigma_1/\sigma_0}{(n+1) + n \cdot \sigma_1/\sigma_0}, \tag{20}$$

where n is the degree of the Legendre polynomial. It is evident that both K_{21} and C_n are only sensitive to the ratio of conductivities, not the absolute values.

The result that scaled conductivities generate the same magnetic field holds for all measurements irrespective of whether they are acquired inside or outside the earth. In addition, for surface MMR data, there is the complication that the magnetic fields from a 1-D earth are the same as those arising from a half-space. This does not mean that the anomalous signal from a buried conductor is independent of the background. In particular, sufficiently conductive overburden can completely shield the body. Nevertheless, we expect to obtain a poor understanding concerning the vertical variation of conductivity from only surface measurements. To illustrate this, consider the anomalous surface field B_y resulting from a cube buried in different 1-D conductivities. The cross-section of the 3-D model is shown in Fig. 5(d). The conductivities of the first layer and the 3-D cube are unchanged for three models, but the conductivity of the second layer varies from 0.001 to 0.1 S m^{-1}. The corresponding anomalous B_y components at the surface are displayed in Figs 5(a)–(c). As the conductivity of the second layer increases, the amplitude of B_y decreases significantly from about 80 to 12 pT. Two factors contribute to this change. As mentioned earlier, the magnetic field is related to the ratio of the conductivities. In this example, the ratio σ_b/σ_2 decreases from 100 to 1, certainly causing a major reduction of the B_y field. At the same time, the magnetic field is also proportional to the amount of anomalous current flowing in the 3-D body, and this is controlled by the 1-D background conductivity. In addition, we see that the three B_y responses have identical shapes, quite similar to a dipole field, and the major difference is only the amplitude. This suggests that it is unlikely that we can distinguish a 3-D body in a layered earth or in a uniform half-space if only the surface MMR data are used.

3 3-D INVERSION OF MMR DATA

As shown in the previous section, the magnetic field $\mathbf{B}^g$, or $\mathbf{B}^a$, is nonlinearly related to the conductivity σ. The goal of the inverse problem is to find a conductivity distribution that can reproduce the observed data to a desired degree. It is well known that the inverse problem is not unique. There are generally infinitely many conductivity models that can fit the observed data equally well. To find a particular model, we can formulate the inverse problem as an optimization problem where an objective function of the model is minimized subject to a constraint that the misfit between the observed and the predicted data is in a desired value. We will briefly outline this approach below.

For MMR inversion, the first question that arises concerns the definition of the 'model' parameter. Conductivity is a positive quantity that can vary by orders of magnitude. We thus define the model parameter as $m = \ln\sigma$. We next construct a model objective function ϕ_m. Our choice for ϕ_m is guided by the fact that we often wish to find a model that has minimum structure in the three spatial directions, and at the same time is close to the reference model m_0. An objective function that has the flexibility to accomplish these goals is

$$\begin{aligned}\phi_m(m, m_0) = \alpha_s \int_v [m(\mathbf{r}) - m_0]^2 \, dv + \alpha_x \int_v \left\{ \frac{\partial [m(\mathbf{r}) - m_0]}{\partial x} \right\}^2 dv \\ + \alpha_y \int_v \left\{ \frac{\partial [m(\mathbf{r}) - m_0]}{\partial y} \right\}^2 dv \\ + \alpha_z \int_v \left\{ \frac{\partial [m(\mathbf{r}) - m_0]}{\partial z} \right\}^2 dv,\end{aligned} \tag{21}$$

where α_s, α_x, α_y and α_z are coefficients that affect the relative importance of different components in the function.

The form of objective function is particularly appropriate for an MMR investigation. With the choice of $m = \ln\sigma$, then $m - m_0 = \ln(\sigma/\sigma_0)$. If σ_0 is a constant, then σ/σ_0 reflects the information that is available from the MMR data alone, namely that the MMR data are not sensitive to the absolute conductivity but are indeterminate by a constant factor. In the absence of *a priori* information we can obtain information only about σ/σ_0. The final conductivity obtained from inversion will be 'floating' on this constant reference conductivity. If σ_0 happens to be the conductivity of the real background geology, the inverted $\sigma(x, y, z)$ might be a good approximation to the conductivity distribution of the true geological model. Otherwise, $\sigma(x, y, z)$ can only reveal the relative conductivity variations with respect to the reference model provided.

To perform a numerical implementation, we discretize the model objective function in eq. (21) using a finite-difference approximation according to the mesh defining the conductivity model. The discrete form of eq. (21) is

$$\phi_m(\mathbf{m}) = \|\mathbf{W}_m(\mathbf{m} - \mathbf{m}_0)\|^2 . \tag{22}$$

The derivation of the matrix $\mathbf{W}_m$, which has incorporated the smallest and three derivative components, can be found in Li & Oldenburg (1996).

The next step in setting up the inversion is to define a data misfit between the observed and predicted data. With the same model parametrization, the forward modelling operator is assumed to be written as $\mathbf{d} = F[\mathbf{m}]$, and we can use the 2-norm measure as the data misfit

$$\phi_d = \left\| \mathbf{W}_d(\mathbf{d} - \mathbf{d}^{obs}) \right\|^2 , \tag{23}$$

where $\mathbf{W}_d$ is a diagonal matrix. If the noise contaminated in the ith observation is an uncorrelated Gaussian random variable having zero mean and standard deviation ε_i, then an appropriate form for $\mathbf{W}_d$ is $\mathbf{W}_d = \mathrm{diag}\{1/\varepsilon_1, \ldots, 1/\varepsilon_N\}$, where N is the number of observations. This assumption makes ϕ_d a random variable distributed as chi-squared with N degrees of freedom, and thus the expected value of ϕ_d is approximately equal to N, assuming the errors are correctly estimated. Therefore, our target misfit ϕ_d^* for the model sought from the inversion should be set around this value.

The inverse problem is now formulated as the optimization problem: minimize an objective function

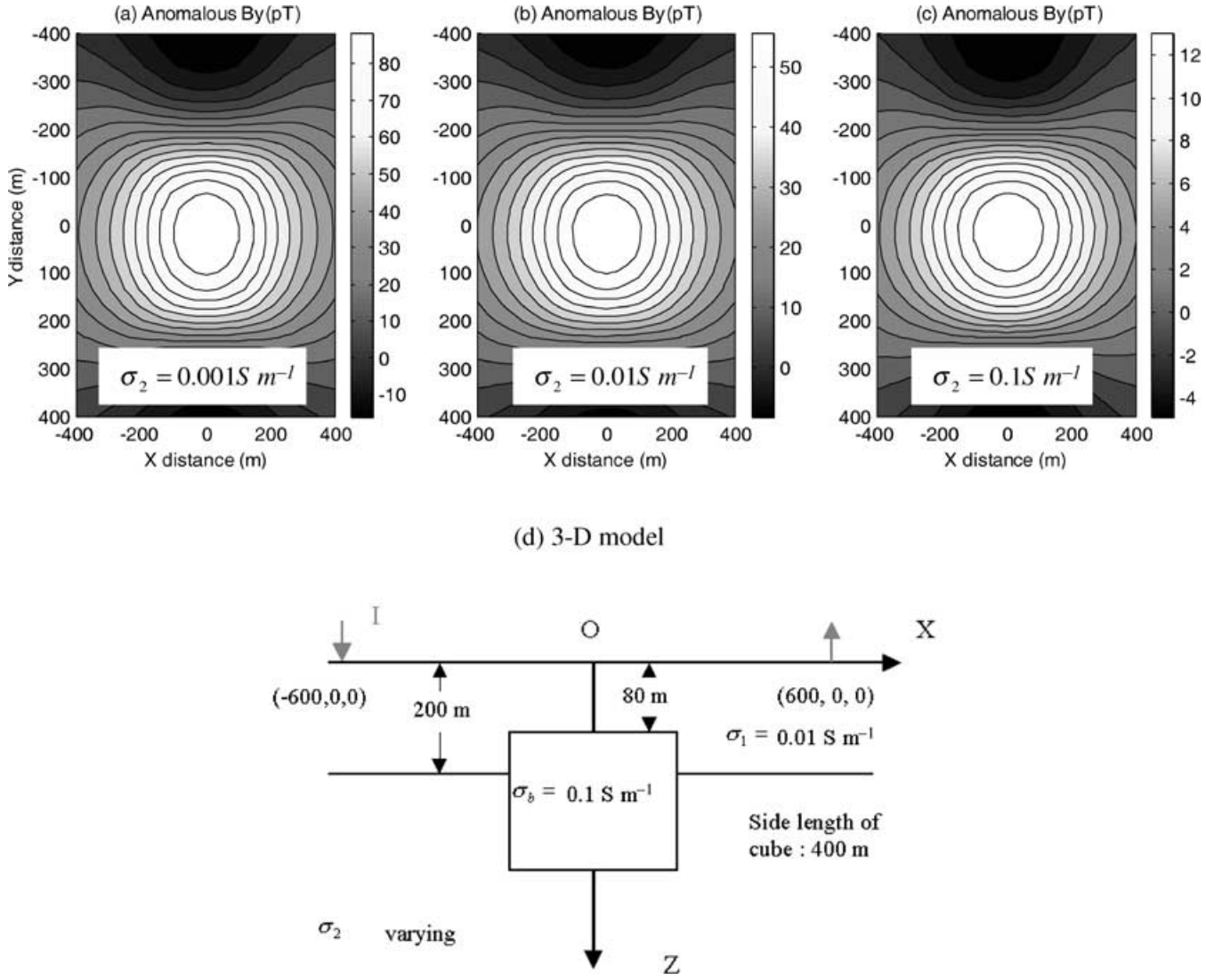

Figure 5. *y*-components of the anomalous magnetic field at the surface produced by 3-D models shown in (d). The conductivity of the basement varies: (a) 0.001 S m^{-1}; (b) 0.01 S m^{-1}; and (c) 0.1 S m^{-1}.

$$\phi(\mathbf{m}) = \phi_{\mathrm{d}} + \beta\phi_m(\mathbf{m}), \tag{24}$$

where β is a regularization parameter.

This problem is non-linear and iteration is required. We use a standard Gauss–Newton approach. At each iteration a model perturbation $\delta\mathbf{m}$ is found by solving

$$\left(\mathbf{J}^{\mathrm{T}}\mathbf{W}_{\mathrm{d}}^{\mathrm{T}}\mathbf{W}_{\mathrm{d}}\mathbf{J} + \beta\mathbf{W}_m^{\mathrm{T}}\mathbf{W}_m\right)\delta\mathbf{m} = -\mathbf{J}^{\mathrm{T}}\mathbf{W}_{\mathrm{d}}^{\mathrm{T}}\mathbf{W}_{\mathrm{d}}\left\{F\left[\mathbf{m}^{(n)}\right] - \mathbf{d}^{\mathrm{obs}}\right\} - \beta\mathbf{W}_m^{\mathrm{T}}\mathbf{W}_m\left(\mathbf{m}^{(n)} - \mathbf{m}_0\right), \tag{25}$$

where $\mathbf{J}$ is the sensitivity matrix (or Jacobian matrix) of $N \times M$, having elements

$$J_{ij} = \frac{\partial d_i}{\partial m_j}. \tag{26}$$

Details regarding the calculation of $\mathbf{J}$, and the product of $\mathbf{J}$ or its transpose with a vector, will be postponed to an appendix. The choice of regularization parameter β has been addressed by many researchers. We adopt a simple cooling procedure in which β starts at a large value and is slowly reduced. We choose an initial β_0 that is sufficiently large so that $\beta_0\mathbf{W}_m^{\mathrm{T}}\mathbf{W}_m$ dominates the $\mathbf{J}^{\mathrm{T}}\mathbf{J}$ component in eq. (25) and hence the problem is nearly quadratic. At the $(k+1)$th iteration we set

$$\beta_{k+1} = \lambda\beta_k, \tag{27}$$

where λ is a constant, usually chosen to be about 0.5. We solve eq. (25) for $\delta\mathbf{m}$ and form

$$\mathbf{m}_{k+1} = \mathbf{m}_k + \alpha\delta\mathbf{m}, \tag{28}$$

where α is a constant step length. A weak line search, initiated by setting $\alpha = 1$, is used to estimate α. This constitutes an inner-loop iteration and the maximum number of iterations is limited to 8. For any α, the updated model $\mathbf{m}_{k+1}$, and associated β_{k+1}, are accepted if the consistency condition (Haber & Oldenburg 2000)

$$\phi_{\mathrm{d}}^{k+1} + \beta_{k+1}\phi_m^{k+1} < \phi_{\mathrm{d}}^{k} + \beta_{k+1}\phi_m^{k}, \tag{29}$$

is satisfied. That is, the updated method results in a reduced value for the objective function. If this inequality is not satisfied, we conclude that the reduction in β_{k+1} has been too large. We therefore increase λ and begin from eq. (27). This process is repeated until the target misfit is achieved.

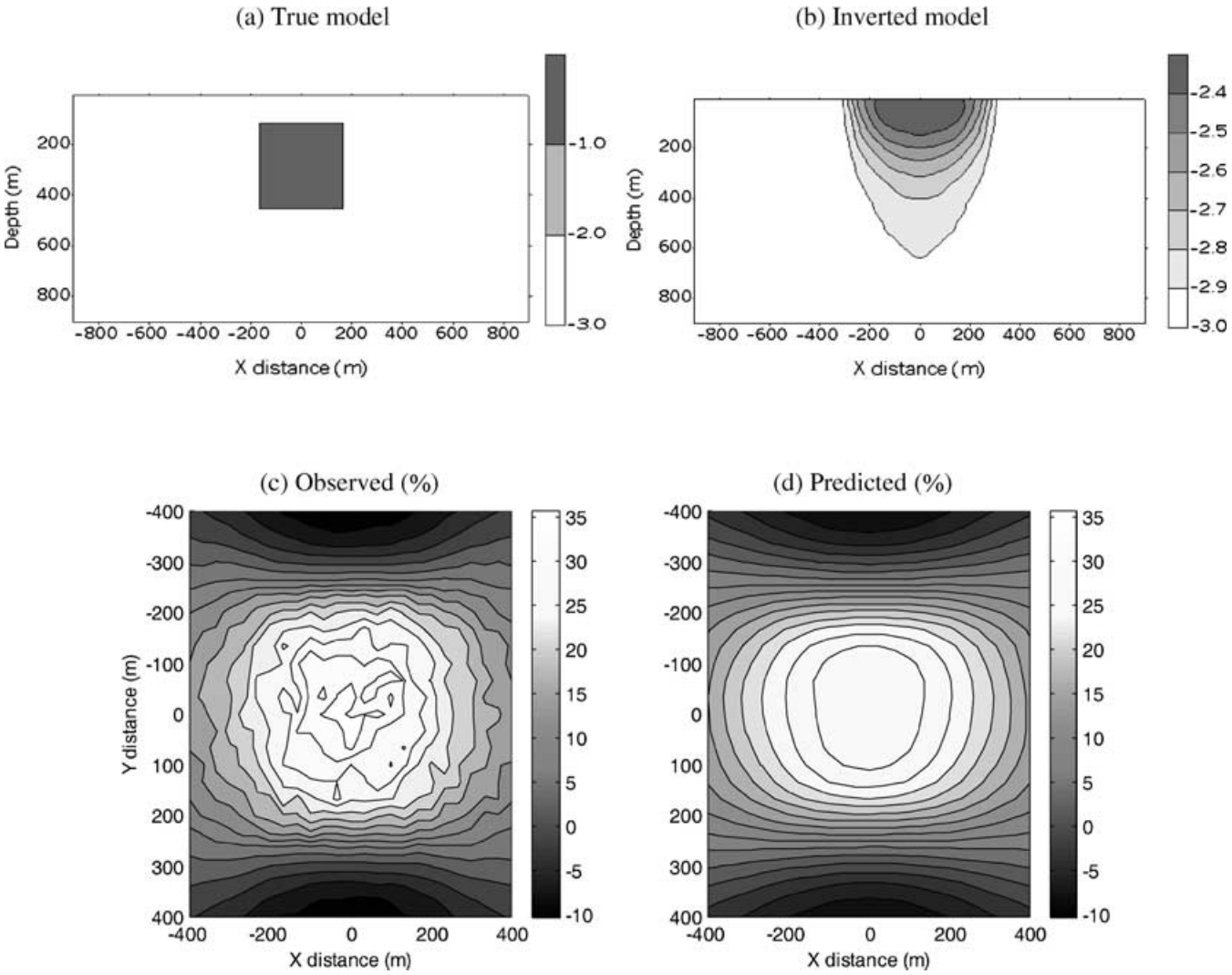

Figure 6. 3-D inversion results of a synthetic MMR anomaly (*y*-component) without depth weighting. The true model is the same as that described in Fig. 1. (a) Cross-section through the centre of the cube; (b) cross-section of the inverted model. The reference model is a half-space of 0.001 S m^{-1}. The greyscales beside both indicates the conductivity (S m^{-1}) in a logarithmic scale. (c) The synthetic anomaly produced by the cube model. Uncorrelated Gaussian noise, with a standard deviation of 5 per cent of the datum magnitude plus 0.5, is added to form the data; (d) the predicted data produced by the inverted model. The greyscales on the bottom two plots show the MMR anomaly as a percentage.

Now we need to address how to solve the matrix equation in eq. (25) for the perturbation $\delta\mathbf{m}$ at each iteration. Solving eq. (25) is identical to solving the equivalent least-squares problem

$$\begin{pmatrix} \mathbf{W}_{\mathrm{d}}\mathbf{J} \\ \sqrt{\beta}\mathbf{W}_m \end{pmatrix} \delta\mathbf{m} = \begin{pmatrix} -\mathbf{W}_{\mathrm{d}}\left(F\left[\mathbf{m}^{(n)}\right] - \mathbf{d}^{\mathrm{obs}}\right) \\ -\sqrt{\beta}\mathbf{W}_m\left(\mathbf{m}^{(n)} - \mathbf{m}_0\right) \end{pmatrix}. \tag{30}$$

We use the conjugate gradient least-squares algorithm (CGLS) (Golub & van Loan 1996) to solve eq. (30). The main computations required for this algorithm are the product of the matrix $\mathbf{J}$ with a vector and the product of the its transpose matrix $\mathbf{J}^{\mathrm{T}}$ with a vector. The derivation is carefully explained in the Appendix.

4 PRACTICAL CONSIDERATIONS OF THE INVERSION

4.1 Depth weighting

As the first example of synthetic data study, we invert the single-component MMR anomaly data (*y*-component) as defined in the previous section. The model consists of a 3-D cube buried in a uniform half-space. The conductivities of the cube and half-space are set to be 0.1 and 0.001 S m^{-1}, respectively. For simplicity, the cube is located right below the origin of the coordinates, with a top depth of 80 m and a side length of 400 m. Fig. 6(a) shows the cross-section of the true model at the $y = 0$ plane. The source and sink electrodes are located at -600 and 600 m along the *x*-axis. The measurement area at the surface extends from -400 to 400 m in both directions, with 25 survey lines and 25 sites on each line, resulting in a total number of 625 data points. The cube produces the MMR anomalies that are shown in Fig. 6(c). The MMR anomaly is obtained by normalizing the anomaly magnetic field (*y*-component here) by the normal field B^{n} at the centre of the survey area, defining the so-called 'MMR anomaly' as a percentage,

$$\text{MMR anomaly} = 100 \times \frac{B^{\mathrm{a}}}{B^{\mathrm{n}}}. \tag{31}$$

The data have independent Gaussian noise added, the standard deviation of which is equal to 5 per cent of the accurate datum plus a constant error of 0.5 pT. We invert these 625 noise-contaminated

data to recover the conductivity of an earth model parametrized by $32 \times 32 \times 15$ cells (the air layer is excluded). The reference model is the same as the true uniform half-space of 0.001 S m^{-1}. After seven iterations, the final misfit is 586 and the cross-section through the centre of the recovered model is shown in Fig. 6(b). The predicted MMR data are also shown in Fig. 6(d) for comparison with Fig. 6(c).

The inverted conductivity model tends to be concentrated near the surface of the earth. The contrast in conductivity between the target and the host (0.6 in a log scale) is also much smaller than the true value of 2 (or 100:1 on a linear scale). These results may have been anticipated because of the close relationship between the magnetic field owing to a volume current distribution and the gravity field owing to a volume density variation. The magnetic field **B** is obtained by the Biot–Savart law, which is given by

$$\mathbf{B} = \frac{\mu}{4\pi} \int_v \mathbf{J} \times \nabla \left(\frac{1}{r} \right) dv, \tag{32}$$

while the gravity field **g** is given by

$$\mathbf{g} = G \int_v \rho \nabla \left(\frac{1}{r} \right) dv, \tag{33}$$

where G is the universal gravitational constant and ρ is the density. Both have the same kernel function $\nabla(1/r)$. When expanding eq. (32), it is easy to find that each component of **B** can be expressed as a linear combination of two components of the gravity field. For example, the B_y component can be written as $B_y = g_x - g_z$, provided that the density ρ is replaced with $\frac{\mu}{4\pi G} J_z$ when computing g_x and with $\frac{\mu}{4\pi G} J_x$ when computing g_z. For a 2-D structure, as first recognized by Szarka (1987), $B_y = -g_z$ if the current flows only parallel to the strike direction (x-direction here). Thus the magnetic field can be estimated using existing gravity formulae (Asten 1988).

It is well known that gravity data have no inherent depth resolution. To counteract the geometric decay of the kernels and to distribute the density with depth, Li & Oldenburg (1998) introduce a depth weighting into the model objective function. The established similarity between the magnetic field and gravity allows us to use the same depth weighting for inversion of the MMR data. The weighting is incorporated into the inversion, by altering the model objective function given by

$$\begin{aligned} \phi_m(m, m_0) = \alpha_s & \int_v \{w(z)[m(\mathbf{r}) - m_0]\}^2 \, dv \\ & + \alpha_x \int_v \left\{ \frac{\partial w(z)[m(\mathbf{r}) - m_0]}{\partial x} \right\}^2 dv \\ & + \alpha_y \int_v \left\{ \frac{\partial w(z)[m(\mathbf{r}) - m_0]}{\partial y} \right\}^2 dv \\ & + \alpha_z \int_v \left\{ \frac{\partial w(z)[m(\mathbf{r}) - m_0]}{\partial z} \right\}^2 dv, \end{aligned} \tag{34}$$

where $w(z)$ is the depth weighting function. This is discretized in the same manner as eq. (21).

For a surface MMR survey, the depth weighting $w(z)$, similar to that implemented in Li & Oldenburg (1996), takes the form of $w(z) = 2z_0/(z + z_0)^\gamma$. The parameters z_0 and γ are chosen so that $w^2(z)$ is approximately equal to the decay of the kernels, so $\gamma \approx 1$ emulates the $1/r^2$ decay of gravity kernels. z_0 depends upon the cell size and the observation height (if there is topography). Here we choose z_0 to be half the thickness of the cell just below the surface, z is the depth to a cell centre, and $\gamma = 0.95$.

We have tested the weighting functions by inverting the noise-contaminated data from the buried cube in the first example. z_0 is equal to 10 m. The reference model is the uniform half-space of 0.001 S m^{-1}. Fig. 7 shows the cross-section through the centre of the inverted conductivity model, which can be compared with Fig. 6(a). The model recovered with the depth weighting is shifted to depth and approximately coincides with the true model. The outline of the constructed model is in reasonable agreement with the true model, and the contrast of the conductivities is increased to about 1.5 (on a log scale), which is much closer to the true contrast of 2.

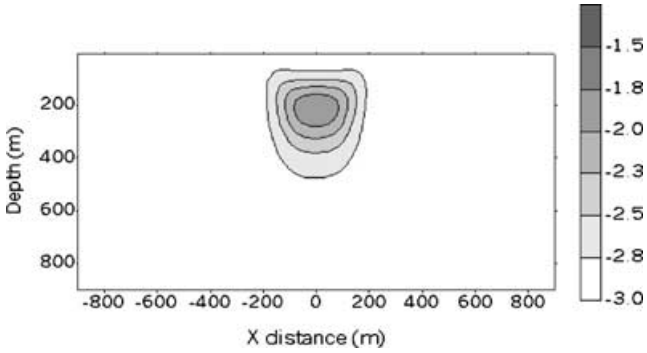

Figure 7. Cross-sections through the centre of the inverted model using the y-component data. The true model is shown in Fig. 6(a). The inversion uses the depth-weighting function discussed in the text. The reference model is a half-space of 0.001 S m^{-1}.

4.2 Issues related to reference model

The choice of reference model is another key element in our inversion algorithm. As explained in the previous section, the MMR anomaly is only sensitive to the relative conductivity contrast between targets and their surroundings. Therefore, the inverted model must be interpreted in conjunction with the reference model. In order to reveal the true conductivity structures, the reference model should be as close to the true background as possible. Without this knowledge of the background to calibrate the models, however, the MMR inversion can still provide useful information concerning the relative conductivity contrast. We use the following example to illustrate this point.

We return to the cube model with all inversion parameters being exactly the same as those used in the depth weighting experiment. The only difference is the choice of the reference model. Two reference models are tested. One is a uniform half-space of 0.01 S m^{-1}, the other 0.1 S m^{-1}. The cross-sections of the inverted models through the centre of the true cube model are shown in Figs 8(a) and (b), respectively. For comparison, these results can be judged in conjunction with the true model and the inverted model using the 0.001 S m^{-1} reference model, both of those are shown in Figs 6(a) and 7. Clearly, the shapes of the inverted anomalies are almost identical for the three different models. They all match quite well with the outline of the true cube. Although the conductivity values shown in the grey bar are changed with the reference models, the contrast (1.5 on a log scale) is almost maintained. This verifies that the choice of constant for a reference model does not affect the recovery of the conductivity contrast structure in our inversion.

The effect of a conductive overburden on the MMR inversion is closely related to the choice of reference model. Suppose that there is a moderately conductive overburden overlying a basement in which a target resides. Surface measurements are acquired with the goal of recovering structures below the overburden. There are two practical issues to be addressed. First, can a significant MMR response from

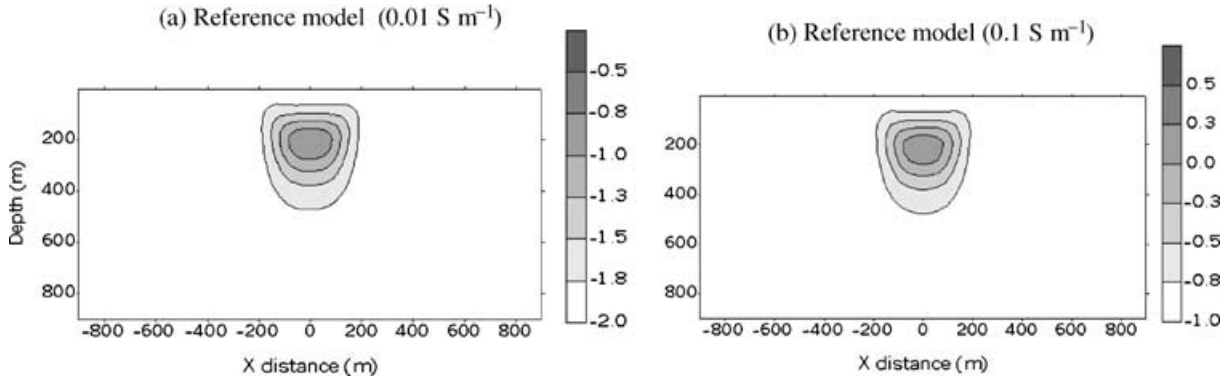

Figure 8. Cross-sections through the centre of the inverted models with a reference model of (a) 0.01 S m^{-1} and (b) 0.1 S m^{-1}. Note the inverted conductivity values, denoted as a logarithm, change with the reference models, but the relative conductivity contrast is principally unchanged.

the target be obtained in the presence of the conductive overburden. In the conventional DC electrical survey, the 'masking effect' has severely limited application in areas where the conductivity of an overburden or weathered layer is one or more orders of magnitude higher than the conductivity of the underlying rock. The second aspect addresses the question of whether the relative conductivity structure of the target can be recovered even though a uniform half-space is specified as the reference model.

To obtain some insight concerning the first issue, we take the cube model as an example, but add an overburden with conductivity of 0.01 S m^{-1} and thickness of 30 m. Other geometric and electrical parameters remain unchanged. Figs 9(a) and (b) show the *y*-component of the anomalous magnetic field for the models without, and with, the conductive overburden, respectively. The maximum magnitude of the magnetic field decreases from 72 to 65 pT, a change of only about 10 per cent. This indicates that we may 'see' the target of interest through a moderately conductive cover layer, and this constitutes a principal advantage of the MMR survey versus the direct current resistivity method. The signal strength for the DC electrical potentials decreases by 50 per cent in this same example.

To address the second question, we invert the MMR data produced from the cube model with the conductive overburden. The data are first contaminated with random Gaussian noise of 5 per cent, the depth weighting is imposed, and the conductivity of the reference model is 0.001 S m^{-1}. A cross-section of the recovered structure in Fig. 10(b), shows that the location of the target and conductivity contrast with the background are reasonably well defined. The inversion provides no indication of the 1-D overburden structure. This is a practical consequence of the fact that surface data from any 1-D conductivity structure is the same as that of a uniform half-space. The reconstruction of the target body, however, has been good because the conductive overburden has not greatly changed the amount and distribution of current going through the prism. When the overburden is thicker, or more conductive, its effect will become more pronounced. In such cases, the choice of reference model becomes more critical. Quantifying these effects is left for future research.

4.3 Which component data to invert?

In the previous synthetic examples, we inverted only the *y*-component of the anomalous MMR response. The choice was tied to practical signal-to-noise ratio issues. With the typical acquisition of MMR data using a horseshoe current layout for the wires, then

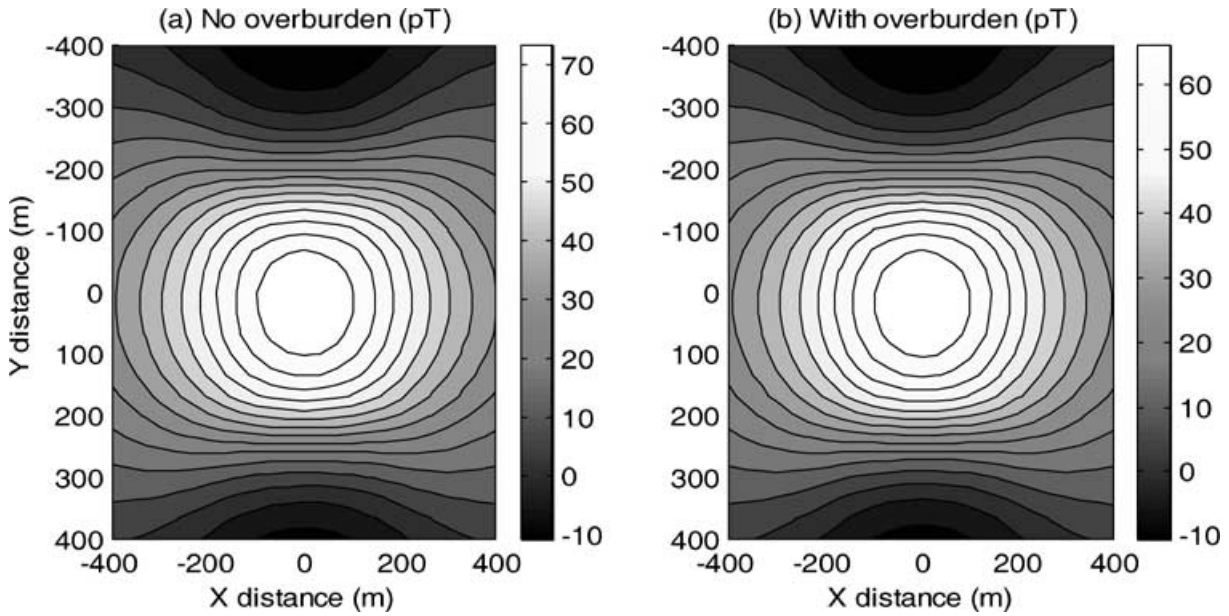

Figure 9. Synthetic *y*-components of the anomalous magnetic field for the cube model: (a) without and (b) with a 30 m thick conductive overburden of 0.01 S m^{-1}. The magnitudes of the magnetic field are in pT. The conductive overburden reduces the anomalous field only by 10 per cent.

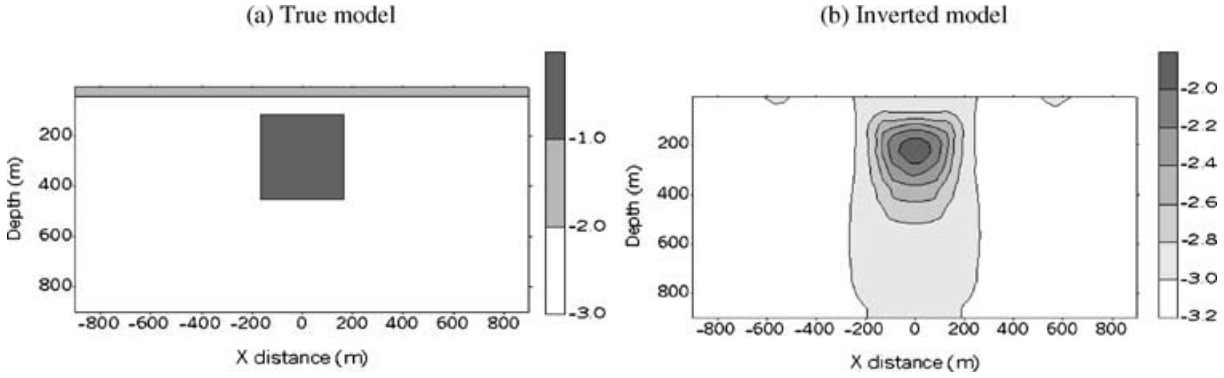

Figure 10. Cross-sections through the centre of the true model with a conductive overburden (a) and of the inverted model (b) obtained by inverting the *y*-component data. The depth weighting function is applied, and the reference model is a half-space of 0.001 S m^{-1}.

the *y*-component of the anomalous magnetic field usually has the highest fidelity. This can be understood as follows.

As explained in the forward modelling section, the total magnetic field consists of three parts: $\mathbf{B}^{w}$, $\mathbf{B}^{n}$ and $\mathbf{B}^{a}$. The magnetic field $\mathbf{B}^{w}$ owing to current flow in the wire can be obtained directly through the Biot–Savart law. For the case of our cube model, the horseshoe wire has three segments, each of those is 1200 m long, and is assumed to be laid on the side of $y < 0$. Because the measurements are made at the surface, $\mathbf{B}^{w}$ only has a vertical component. The other two horizontal components are null. Deviations of the wire into the vertical direction will generate horizontal components. It is for this reason that the U-shape was adopted so that the wire is away from the location at which fields are to be measured. In contrast, the normal magnetic field $\mathbf{B}^{n}$ has no vertical component, but just two horizontal components, which can be calculated analytically. The anomalous magnetic fields $\mathbf{B}^{a}$ have been shown in Fig. 1. Adding $\mathbf{B}^{w}$, $\mathbf{B}^{n}$ and $\mathbf{B}^{a}$ generates the total magnetic field for each component. These are shown in Fig. 11. This figure clearly shows that B_z has the largest amplitude of about 1200 pT; the second is B_y, 650 pT, and the least is B_x, 200 pT. From the viewpoint of measurements, B_z has the highest signal strength and thus it might be the best one to invert. However, only the anomalous field components contain useful information concerning the target of interest and so we invert them. From Fig. 1, the amplitudes for the vertical and *y*-component of the anomalous fields are about the same size, 60 and 70 pT, respectively; the *x*-component is roughly one-third of the *y*-component. Thus, B_z and B_y have the largest anomalous signal strength. In practice, the layout of the wire along the three sides may be not straight, or the surface of the earth is not a flat as it is supposed to be. Both situations will make B_z more noise-prone compared with B_y and hence it is usually only the B_y component, which is collected and inverted. In principle, however, if the location of the current wire is recorded accurately, then its effect can be subtracted and all components contain valuable information concerning the subsurface conductivity variations. As an illustration Fig. 12 shows the cross-section of the recovered conductivity model obtained by inverting only the vertical component data. Gaussian noise of 5 per cent plus a floor error of 0.5 pT was added to the data prior to inversion. Both the location of the cube and the conductivity contrast are reasonably well defined, and the recovered model compares favourably with that shown in Fig. 10(b).

5 FIELD EXAMPLE

Surface MMR data were collected at the Mons Cupri deposit of the Pilbara area, Western Australia. As shown in Fig. 13, the general strike of the formation around the Mons Cupri deposit is north–south and dips 30° westward. The ore body is hosted by the Mons Cupri rhyolite fragmental, which is sequentially overlain by the Cistern Formation, Cap shale, Comstock andesite and Whim Creek shale.

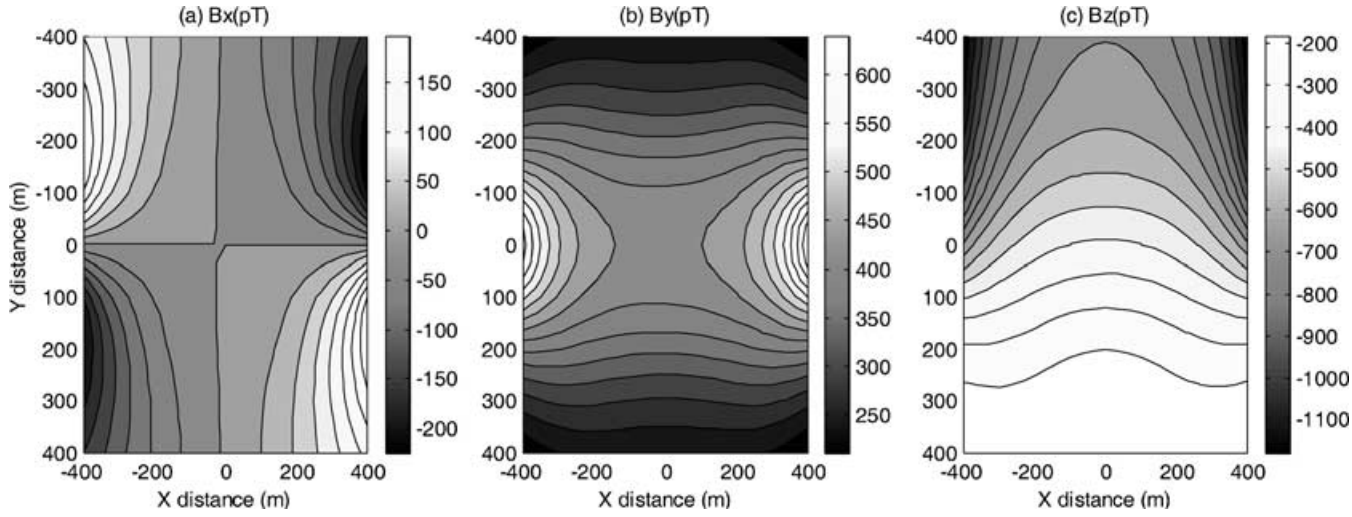

Figure 11. The total magnetic fields produced by the cube model, which are composed by three parts: $\mathbf{B}^{w}$, $\mathbf{B}^{n}$, and $\mathbf{B}^{a}$. $\mathbf{B}^{a}$ is shown in Fig. 1.

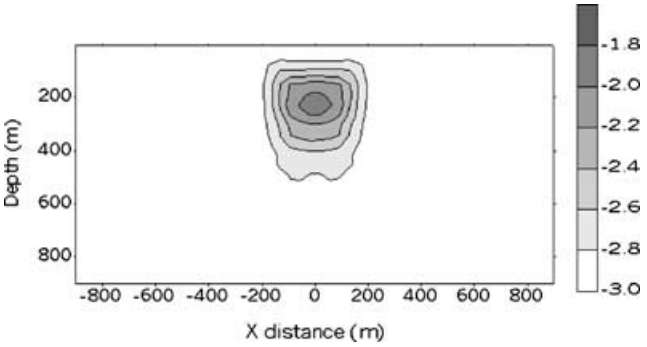

Figure 12. Cross-sections through the centre of the inverted model by inverting the z-component data. The true model is shown in Fig. 10(a). The depth weighting function is applied, and the reference model is a half-space of 0.001 S m^{-1}.

Mineralization consists of a zone of iron-rich chlorite and carbonate alteration containing disseminated and stockwork chalcopyrite mineralization overlain by a shallowly dipping massive sphalerite galena, chalcopyrite lens in volcaniclastic and cherty sediments (Linford 1990). The stockwork zone, containing copper mineralization in chalcedonic silica and carbonate veins, dips steeply to the south, and is approximately 1 km long, extending to 200 m below the present surface. The uppermost part of the ore body is oxidized down to 100 m below the surface. It has been estimated that the deposit's resource is 1.5 Mt oxide ore at 1.13 wt per cent Cu and 1.4 Mt sulphide ore at 1.74 wt per cent Cu, 1.13 wt per cent Pb and 2.48 wt per cent Zn.

MMR surveys, together with MIP, were conducted over the deposit by Scintrex (Linford 1990). The current electrodes were set on 1000N at 1500E and 300E, and are aligned with the geological cross-section. An area of 1000 m × 1000 m over the ore body was surveyed. 11 survey lines parallel to the strike were 100 m apart, and the station interval inside the central 500 m × 500 m area was 50 m and it was 100 m outside this central area. Data were acquired at 0.3 Hz. The observed horizontal magnetic field (south-pointing) was reduced to the MMR response in per cent by the procedure discussed earlier. Fig. 14(a) shows the MMR responses at the 162 stations. Basically, there are two regions where the MMR response is high. One, at line 1400N, extends from 500E to 800E, and has a magnitude of about 104 per cent. From Fig. 13, this anomaly is approximately coincident with the surface expression of the marked Cu gossan and mineralization at the upper left-hand corner. The other MMR high is much smaller and is located at about 950N, and extends from 1100E to 1250E. Interestingly, this anomaly is directly above the known massive sulphides. These two highs suggest that the mineralization is more conductive compared with its surroundings. Other local highs may be not trustworthy because only a single data point is involved. There is a large negative anomaly at 1000N of the West side of survey area. The anomaly is as low as −162 per cent, indicating a more resistive structure than the host medium.

The survey area is characterized by a flat terrain except for the small scattered hills resistant to the erosion, so a 3-D model of $2 \times 2 \times 1$ km^3 (excluding the air space), without topography, was designed. The model was discretized horizontally at a non-uniform interval, from 50 m in the central 1000 m × 1000 m area, to 100 m outside. In the vertical direction, the first 300 m was divided at a 25 m interval so that the shallow structure could be adequately modelled. Below that, an interval of 50–100 m was used. This resulted in a mesh with $34 \times 34 \times 20$ cells. The inverse problem was therefore formalized by inverting 162 data points to recover the conductivities in these 23 120 cells. The reference model was a uniform half-space of 0.001 S m^{-1}. Little is known concerning the conductivity of the different rock units but they are probably resistive. Two core sample measurements exist (Linford 1990). The resistivity of a copper-disseminated sulphide and oxide sample is 3000 Ω m, while a copper-massive sulphide sample is less than 1 Ω m. For the inversion, a depth-weighting function with $\gamma = 0.95$ and $z_0 = 12.5$ m was adopted. We also assumed that each datum had an error whose standard deviation was equal to 8 per cent of its magnitude plus a base value of 2 anomaly units. The target misfit was set to 162, but the achieved misfit after 13 iterations was 850. Most of the misfit comes from the isolated points such as that at the upper right-hand corner. The predicted data are shown in Fig. 14(b).

The recovered conductivity model is shown in Fig. 15 as one plan-section at a depth of 85 m. There are four regions of anomalously high conductivity. Two regions at (1400N, 600E) and (1000N, 1100E) correspond to known ore deposits. The dotted circles indicate surface locations of the deposits inferred from geology. The maximum recovered conductivity value is about 58 mS m^{-1}, which is much smaller than the core sample conductivity of 1 S m^{-1} for the massive sulphides. This may be explained in two ways. First, the saturation effect of MMR responses prevents the algorithm from producing a target whose conductivity value is 100 times greater than its surrounding. In this case, the reference model has a conductivity of 1 mS m^{-1}, and thus the maximum conductivity for any highly conductive target should be less than 100 mS m^{-1}. Secondly, the MMR response on the surface is produced by bulk conductivities for one discretized model. The recovered 'bulk' conductivity of our large prisms is likely to be less than the 'point' core sample value. The other two regions of high conductivity occur at (700N, 1000E) and (1400N, 1400E). We have no information about them. The whitish region in the area (800–1200N, 300–500E) indicated highly resistive material (0.1 mS m^{-1}), which accounts for the negative MMR response on the left-hand side of the central deposit. These highly resistive materials may be associated with Whim Creek shale and some volcanics.

Fig. 16 compares the recovered conductivity model with the geology in the cross-section at 950N. The lead–zinc mineralization consists of two tabular targets separated by about 200 m in depth. The MMR results show a region of high conductivity centred between the two mineralized lenses. This is characteristic of a low-resolution image of a complex structure. Overall, we feel that the inversion has been successful in delineating the volume containing the mineralization, but the resolution is poor. Acquisition of other components of the magnetic field, and especially, obtaining data from one or more other locations of the current electrodes, could greatly improve the results.

6 DISCUSSIONS

We have developed an algorithm to compute the MMR response owing to steady current sources in a 3-D environment. This is achieved in two consecutive steps: first, solving a DC resistivity problem and then solving a magnetostatic subproblem. The differential equations involved in these two problems are solved numerically using the finite-volume technique based on a staggered grid. The algorithm is versatile: the grounded sources can be located anywhere although we assumed the sources were at the surface of the earth in our examples; topography can be included into the model; and highly discontinuous conductivity and susceptibility can also be handled.

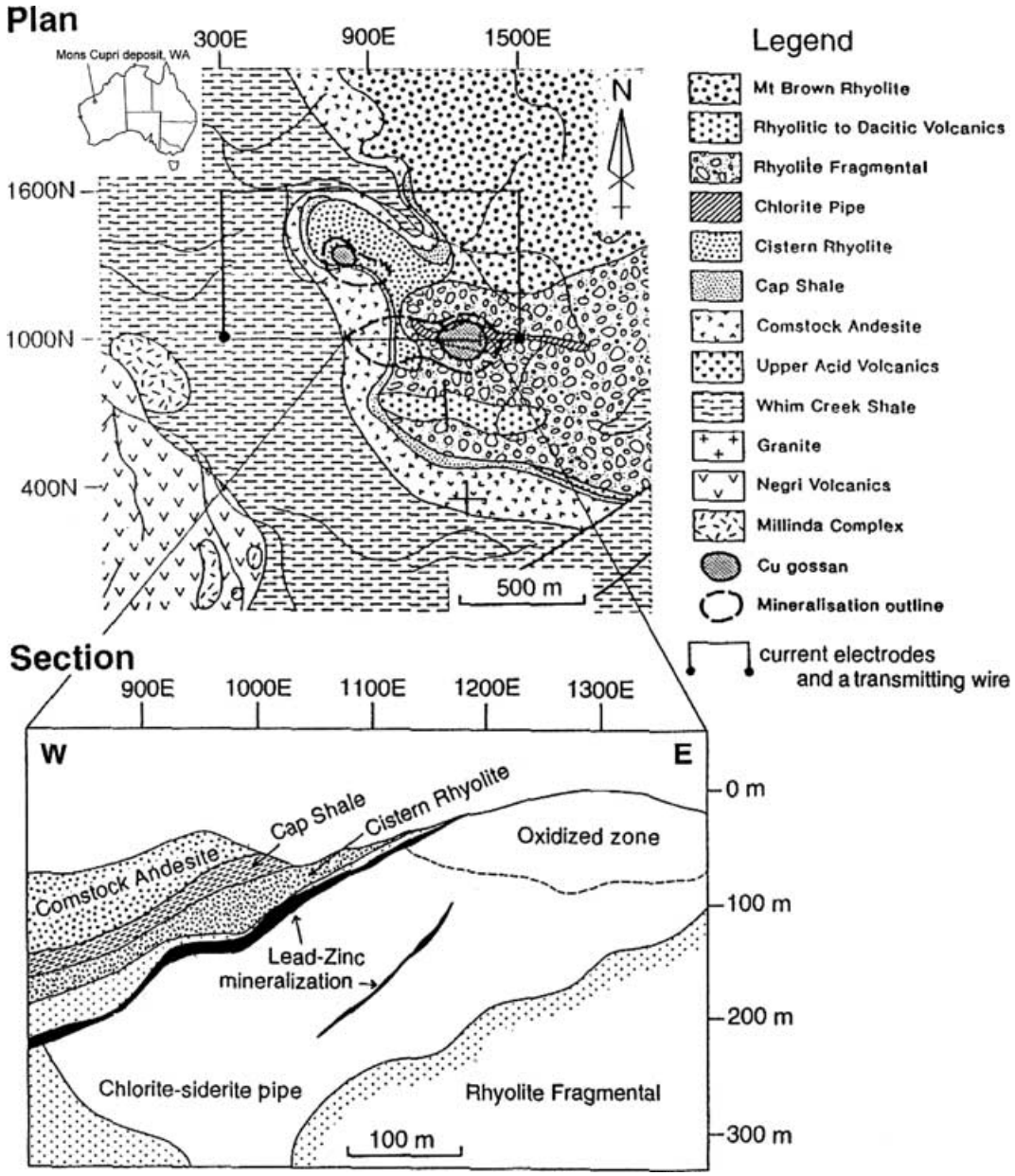

Figure 13. Geological plan and section view of the Mons Cupri deposit with current electrodes, connecting wires and the MMR survey area.

The algorithm has been tested against analytical models such as a vertical contact and hemispherical depression.

We have also developed a technique to invert the surface MMR data to recover a 3-D conductivity distribution. To overcome the inherent non-uniqueness of the inverse problem, we obtain the solution by minimizing a specific model objective function subject to a target misfit. Because the static magnetic field has no depth resolution, a depth-weighting function has to be included into the objective function. The minimization is carried out using the Gauss–Newton method in which the perturbation at each iteration is obtained by solving an equivalent conjugate gradient least-squares problem. A crucial element in solving a large-scale inverse problem is that we avoid computing and storing the sensitivity matrix explicitly; instead, we only need to calculate the sensitivity matrix and its transpose multiplying a vector. This is equivalent to two forward modellings. The regularization parameter controlling the balance between data misfit and model norm is determined pragmatically in a cooling process.

The interpretation of MMR data is made somewhat more difficult because of the fundamental non-uniqueness. That is, the conductivity obtained from inverting MMR data is always ambiguous by a multiplicative constant. Equivalently, the MMR response is only dependent upon the relative conductivity and not the absolute conductivity, and this leads us to formulate the inverse problem in terms of a quantity $\log(\sigma(z)/\sigma_{\text{ref}})$. For a body buried in a uniform host medium we can choose a constant conductivity as a reference model. The choice of constant reference model does not have any effect on the recovery of the relative conductivity structure but if it has been chosen correctly then the final conductivity will have been properly calibrated.

A more complicated scenario is a 3-D body residing in a 1-D layered medium. The 1-D earth is a complicating factor for a number

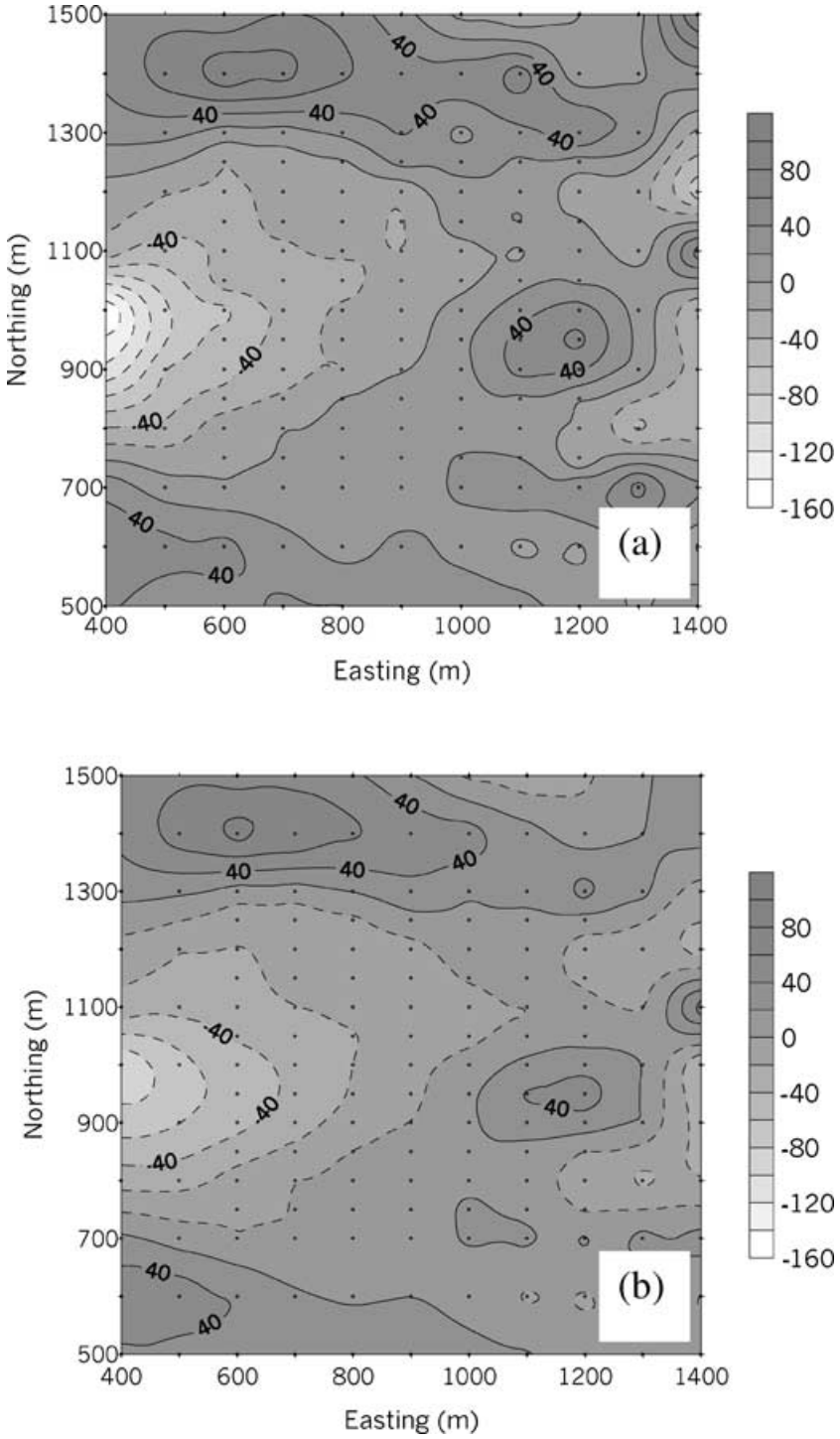

Figure 14. (a) The MMR response (per cent) over the Mons Cupri deposit. The survey area is 1000 m × 1000 m, with a line spacing of 100 m and a station interval of 50 m in the central area and 100 m outside, resulting in 162 stations (marked by dots). See Fig. 13 for reference. The measured data are horizontal (South) components of magnetic field at frequency of 0.3 Hz. (b) The predicted response from the recovered model.

of reasons. First, its surface MMR response is identical to that of a homogenous earth and so there is another source of non-uniqueness in the problem. Secondly, the anomalous signal we measure is not only related to the ratio of conductivity between the 3-D body and its surroundings, but it is also controlled by the conductivity structure of the 1-D earth. This is because the measured signal is proportional to the amount of anomalous current in the body. When the host medium does not change the current distribution in the earth significantly, such as a 3-D body with a thin and moderately conductive overburden, the signal will not be altered much compared with that in a uniform host, and thus it is possible to reconstruct the relative conductivity of the 3-D body. Otherwise, the responses will be altered significantly. Quantifying this interaction effect between the host and the target on the inversion result is a subject for future research.

The work provided here is general. We show how to invert magnetic data that arise from any steady state current. We have presented examples that are associated with a traditional MMR geometry used

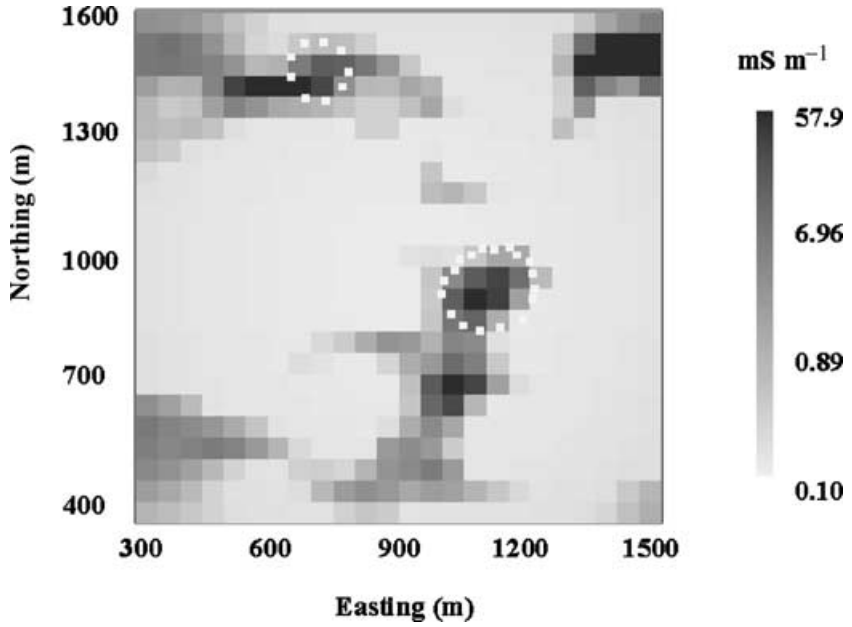

Figure 15. The recovered conductivity model shown in plan-section at a depth of 85 m. The known Cu gossan and mineralization at the surface are also marked.

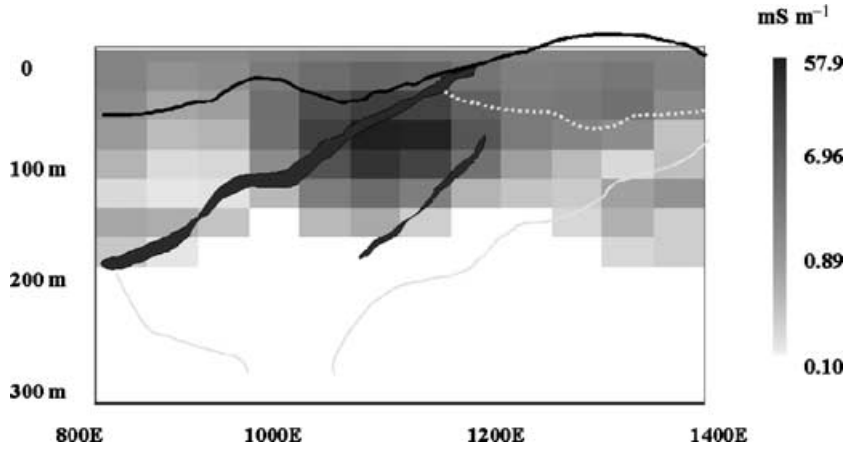

Figure 16. Comparison of the recovered conductivity model in a cross-section (950N) with the geology for the Mons Cupri deposit. The conductivity high is correlated to the deposit, and the resistive basement relates to the Rhyolite Fragmental.

in mineral exploration. The field example was deemed to be successful in that the low-resolution image from the inversion seemed to correspond with the major geological units (in particular, the mineralization), however, it also highlights the deficiencies in the traditional field approach. Only one source location and one component of magnetic field data were used in the inversion. More source locations, and acquisition of full three-component data, would greatly improve the results. We hope that the ability to invert such data will prompt these improved survey techniques.

ACKNOWLEDGMENTS

This work was supported by an NSERC IOR grant and an industry consortium Inversion and Modelling of Applied Geophysical Electromagnetic data (IMAGE) project. Participating companies are Newmont Gold Company, Falconbridge, Placer Dome, Anglo American, INCO Exploration & Technical Services, MIM, Cominco Exploration, AGIP, Muskox Minerals, Billiton, Kennecott Exploration Company. We are grateful to Professors Ralph U. Boerner, Laszlo Szarka and editor Karsten Bahr for their comments and suggestions.

REFERENCES

Acosta, J.E. & Worthington, M.H., 1983. A borehole magnetometric resistivity experiment, *Geophys. Prospect.,* **31,** 800–809.

Asten, M.W., 1988. The downhole magnetometric resistivity (DHMMR) method, *Expl. Geophys.,* **18,** 12–16.

Barrett, R. *et al.*, 1994. *Templates for the Solution of Linear Systems: Building Blocks for Iterative Methods,* SIAM, Philadelphia, PA.

Bishop, J., Carroll, N. & Macinnes, S., 1997. Finding Sphalerite at Broken Hill drillhole magnetometric resistivity, *Expl. Geophys.,* **28,** 6–10.

Boggs, D.B., 1999. The theory and application of sub-audio magnetic data acquisition and numerical modelling, *PhD thesis,* University of New England, Australia.

Boggs, D.B., Stanley, J.M. & Cattach, M.K., 1999. Three-dimensional numerical modelling of sub-audio magnetic data, *Expl. Geophys.,* **30,** 147–156.

Cheesman, S.J. & Edwards, R.N., 1989. Current channelling in square plates with applications to magnetometric resistivity, *Geophy. Prospect.,* **37,** 553–581.

Dey, A. & Morrison, H.F., 1979. Resistivity modelling for arbitrarily shaped three-dimensional structures, *Geophysics,* **36,** 753–780.

Edwards, R.N., 1974. The magnetometeric resistivity (MMR) method and its application to the mapping of a fault, *Can. J. Earth Sci.,* **11,** 1136–1156.

Edwards, R.N. & Nabighian, M.N., 1991. The magnetometric resistivity method, in *Electromagnetic Methods in Applied Geophysics: Investigations in Geophysics,* Vol. 2, pp. 47–104, Part A, Society of Exploration Geophysicists.

Edwards, R.N., Lee, H. & Nabighian, M.N., 1978. On the theory of magnetometric resistivity (MMR) methods, *Geophysics,* **27,** 1176–1203.

Golub, G. & van Loan, C.F., 1996. *Matrix Computations,* The Johns Hopkins University Press, London.

Gomez Trevino, E. & Edwards, R.N., 1979. Magnetometric resistivity (MMR) anomalies of two-dimensional structures, *Geophysics,* **44,** 947–958.

Haber, E., 2000. A mixed finite element method for the solution of the magnetostatic problem with highly discontinuous coefficients in 3D, *Comput. Geosci.,* **4,** 323–336.

Haber, E. & Ascher, U.M., 2001. Fast finite volume modelling of 3D electromagnetic problems with highly discontinuous coefficients, *SIAM J. Sci. Comput.,* **22,** 1943–1961.

Haber, E. & Oldenburg, D.W., 2000. A GCV based method for nonlinear ill-posed problems, *Comput. Geosci.,* **4,** 41–63.

Haber, E., Ascher, U.M. & Oldenburg, D.W., 2000a. Fast simulation of 3D electromagnetic problems using potentials, *J. Comp. Phys.,* **163,** 150–171.

Haber, E., Ascher, U.M. & Oldenburg, D.W., 2000b. On optimization techniques for solving non-linear inverse problems, *Inverse Problems,* **16,** 1263–1280.

Howland-Rose, A.W., Linford, G., Pitcher, D.H. & Seigel, H.O., 1980. Some recent magnetic induced-polarization development—Part 2: Survey results, *Geophysics,* **45,** 55–74.

Inayat-Hussein, A.A., 1989. Magnetic fields of direct currents in horizontally stratified conductors, *J. appl. Phys.,* **65,** 3731–3732.

Jin, J., 1993. *The Finite Element Method in Electromagnetics,* John Wiley and Sons, New York.

Li, Y. & Oldenburg, D.W., 1996. 3-D inversion of magnetic data, *Geophysics,* **61,** 394–408.

Li, Y. & Oldenburg, D.W., 1998. 3-D inversion of gravity data, *Geophysics,* **63,** 109–119.

Linford, G., 1990. Report on a magnetic induced polarization survey, Mons Cupri and Salt Creek deposits, near Whim Creek, W.A., Scintrex report (unpublished).

Nabighian, M.N., Oppliger, G.L., Edwards, R.N., Lo, B.B.H. & Cheesman, S.J., 1984. Cross-hole magnetometric resistivity (MMR), *Geophysics,* **49,** 1313–1326.

Oppliger, G.L., 1984. Three-dimensional terrain corrections for mise-a-la-masse and magnetometric resistivity surveys, *Geophysics,* **49,** 1718–1729.

Pai, D. & Edwards, R.N., 1983. Programme MMR2DFD: finite difference modelling of MMR anomalies: Res., in *Applied Geophysics,* Vol. 25, University of Toronto.

Szarka, L., 1987. Geophysical mapping by stationary electric and magnetic field components: a combination of potential gradient mapping and magnetometric resistivity methods, *Geophys. Prosp.,* **35,** 424–444.

Van der Vorst, H.A., 1992. BiCGSTAB: A fast and smoothly converging variant of the Bi-CG for the solution of nonsymmetric linear systems, *SIAM J. Sci., Stat. Comp.,* **13,** 631–644.

Yang, C.H. & Tseng, H.W., 1992. Topographic responses in magnetometric resistivity modelling, *Geophysics,* **57,** 1409–1418.

Zhang, J., Mackie, R.L. & Madden, T.R., 1995. 3-D resistivity forward modelling and inversion using conjugate gradients, *Geophysics,* **60,** 1313–1325.

Zhao, S. & Yedlin, M.J., 1996. Some refinements on the finite-difference method for 3-D DC resistivity modelling, *Geophysics,* **61,** 1301–1307.

APPENDIX: COMPUTATION OF $\mathbf{J}\cdot\mathbf{v}$ AND $\mathbf{J}^{\mathrm{T}}\cdot\mathbf{v}$

For convenience, we use a new notation (more details can be referred to Haber *et al.* 2000b)

$$\mathbf{A}(\mathbf{m})\cdot\mathbf{u}=\mathbf{f}, \tag{A1}$$

to simplify the forward modelling matrix systems as given in eq. (11). The coefficient matrix is

$$\mathbf{A}(\mathbf{m})=\begin{pmatrix}\nabla_h^{(e)}\times\mathbf{M}_{\mathrm{e}}^{-1}\nabla_h^{(f)}\times-\nabla_h\mathbf{M}_{\mathrm{c}}^{-1}\nabla_h\cdot & \mathbf{S}\nabla_h\\ 0 & \nabla_h\cdot\mathbf{S}\nabla_h\end{pmatrix}, \tag{A2}$$

the unknown vector

$$\mathbf{u}=\begin{pmatrix}\tilde{\mathbf{A}}\\ \phi\end{pmatrix},$$

and the source vector

$$\mathbf{f}=\begin{pmatrix}\mathbf{J}^s\\ \nabla_h\cdot\mathbf{J}^s\end{pmatrix},$$

where $\tilde{\mathbf{A}}$ is the vector potential. By doing so, the data vector $\mathbf{d}$ can be written as

$$\mathbf{d}=\mathbf{Q}\mathbf{u}, \tag{A3}$$

where $\mathbf{Q}$ is a projection matrix that generates the data from the computed fields. If the $\mathbf{B}$ field is required, $\mathbf{Q}$ can be obtained by multiplying a linear interpolation matrix with the curl matrix $\nabla_h^{(f)}\times$. Therefore, $\mathbf{Q}$ is independent to the model $\mathbf{m}$.

To express the sensitivity matrix $\mathbf{J}$ explicitly in the new notation, we differentiate the discretized differential eq. (A1) with respect to $\mathbf{m}$ (assuming $\mathbf{u}$ is a function of $\mathbf{m}$). This will yield

$$\frac{\partial[\mathbf{A}(\mathbf{m})\mathbf{u}(\mathbf{m})]}{\partial\mathbf{m}}=\frac{\partial[\mathbf{A}(\mathbf{m})\mathbf{u}]}{\partial\mathbf{m}}+\mathbf{A}(\mathbf{m})\frac{\partial\mathbf{u}(\mathbf{m})}{\partial\mathbf{m}}=0. \tag{A4}$$

We take a new matrix $\mathbf{G}(\mathbf{m},\mathbf{u})$ to represent the first term, i.e.

$$\mathbf{G}(\mathbf{m},\mathbf{u})=\frac{\partial[\mathbf{A}(\mathbf{m})\mathbf{u}]}{\partial\mathbf{m}}, \tag{A5}$$

where $\mathbf{u}$ is just a vector and not related to $\mathbf{m}$. Substituting $\mathbf{G}(\mathbf{m},\mathbf{u})$ into eq. (A4) will lead to

$$\frac{\partial\mathbf{u}(\mathbf{m})}{\partial\mathbf{m}}=-\mathbf{A}^{-1}(\mathbf{m})\mathbf{G}(\mathbf{m},\mathbf{u}). \tag{A6}$$

Thus, the sensitivity matrix $\mathbf{J}$ can be written symbolically as

$$\mathbf{J}=\frac{\partial\mathbf{d}}{\partial\mathbf{m}}=\frac{\partial[\mathbf{Q}\mathbf{u}(\mathbf{m})]}{\partial\mathbf{m}}=\mathbf{Q}\frac{\partial\mathbf{u}(\mathbf{m})}{\partial\mathbf{m}}=-\mathbf{Q}\mathbf{A}^{-1}(\mathbf{m})\mathbf{G}(\mathbf{m},\mathbf{u}). \tag{A7}$$

The intermediate matrix $\mathbf{G}(\mathbf{m},\mathbf{u})$ can be derived as follows. From eq. (A2) we see that only the material property matrix $\mathbf{S}$ is related to the model $\mathbf{m}$, therefore

$$\mathbf{G}(\mathbf{m},\mathbf{u})=\frac{\partial[\mathbf{A}(\mathbf{m})\mathbf{u}]}{\partial\mathbf{m}}=\begin{pmatrix}\dfrac{\partial(\mathbf{S}\nabla_h\phi)}{\partial\mathbf{m}}\\ \nabla_h\cdot\dfrac{\partial(\mathbf{S}\nabla_h\phi)}{\partial\mathbf{m}}\end{pmatrix}. \tag{A8}$$

Because $\mathbf{S}$ is a diagonal matrix with elements that are the harmonic average of conductivities at the two adjacent cells, $\partial(\mathbf{S}\nabla_h\phi)/\partial\mathbf{m}$ can be obtained analytically without too much work.

The products of the sensitivity matrix and its transpose with a vector are now readily computed. Consider $\mathbf{J}\cdot\mathbf{v}$, where $\mathbf{v}$ is a known vector.

$$\mathbf{J}\cdot\mathbf{v} = -\mathbf{Q}\mathbf{A}^{-1}(\mathbf{m})\mathbf{G}(\mathbf{m},\mathbf{u})\mathbf{v}, \tag{A9}$$

and we can obtain it in three steps. First compute $\mathbf{G}(\mathbf{m},\mathbf{u})\mathbf{v} = \mathbf{q}$. Then calculate $\mathbf{A}^{-1}(\mathbf{m})\mathbf{q} = \mathbf{w}$, which is equivalent to solving the forward modelling problem $\mathbf{A}(\mathbf{m})\mathbf{w} = \mathbf{q}$, addressed in the main body of this paper. Once $\mathbf{w}$ is obtained, the last step is just to multiply $\mathbf{w}$ by $-\mathbf{Q}$, i.e. $\mathbf{J}\cdot\mathbf{v} = -\mathbf{Q}\mathbf{w}$.

Then we turn to deal with $\mathbf{J}^{\mathrm{T}}\mathbf{v}$, which can be expanded as

$$\mathbf{J}^{\mathrm{T}}\cdot\mathbf{v} = -(\mathbf{Q}\mathbf{A}^{-1}(\mathbf{m})\mathbf{G}(\mathbf{m},\mathbf{u}))^{\mathrm{T}}\mathbf{v} = -\mathbf{G}^{\mathrm{T}}(\mathbf{m},\mathbf{u})\mathbf{A}^{-\mathrm{T}}(\mathbf{m})\mathbf{Q}^{\mathrm{T}}\mathbf{v}. \tag{A10}$$

Similarly, we can define $\mathbf{q} = \mathbf{Q}^{\mathrm{T}}\mathbf{v}$, and $\mathbf{w} = \mathbf{A}^{-\mathrm{T}}(\mathbf{m})\mathbf{q}$. This means that $\mathbf{A}^{\mathrm{T}}(\mathbf{m})\mathbf{w} = \mathbf{q}$, i.e.

$$\begin{pmatrix} \left(\nabla_h^{(e)}\times\mathbf{M}_{\mathrm{e}}^{-1}\nabla_h^{(f)}\times -\nabla_h\mathbf{M}_{\mathrm{c}}^{-1}\nabla_h\cdot\right)^{\mathrm{T}} & 0 \\ (\mathbf{S}\nabla_h)^{\mathrm{T}} & (\nabla_h\cdot\mathbf{S}\nabla_h)^{\mathrm{T}} \end{pmatrix}\mathbf{w} = \mathbf{q}. \tag{A11}$$

As mentioned earlier, eq. (A11) can be decoupled into two systems. Let

$$\mathbf{w} = \begin{pmatrix} \mathbf{w}_a \\ \mathbf{w}_\phi \end{pmatrix}$$

and

$$\mathbf{q} = \begin{pmatrix} \mathbf{q}_a \\ \mathbf{q}_\phi \end{pmatrix},$$

then eq. (A11) can be written as

$$\left(\nabla_h^{(e)}\times\mathbf{M}_{\mathrm{e}}^{-1}\nabla_h^{(f)}\times -\nabla_h\mathbf{M}_{\mathrm{c}}^{-1}\nabla_h\cdot\right)^{\mathrm{T}}\mathbf{w}_a = \mathbf{q}_a, \tag{A12a}$$

and

$$(\nabla_h\cdot\mathbf{S}\nabla_h)^{\mathrm{T}}\mathbf{w}_\phi = \mathbf{q}_\phi - (\mathbf{S}\nabla_h)^{\mathrm{T}}\mathbf{w}_a. \tag{A12b}$$

We can first solve for $\mathbf{w}_a$ from eq. (A12a), substitute $\mathbf{w}_a$ into the right-hand side of eq. (A12b), and then solve for $\mathbf{w}_\phi$ from (A12b). Once $\mathbf{w}_a$ and $\mathbf{w}_\phi$ have been computed, $\mathbf{J}^{\mathrm{T}}\mathbf{v}$ can be obtained from

$$\mathbf{J}^{\mathrm{T}}\cdot\mathbf{v} = -\mathbf{G}^{\mathrm{T}}(\mathbf{m},\mathbf{u})\mathbf{w}. \tag{A13}$$

Roughly speaking, computing $\mathbf{J}\cdot\mathbf{v}$ and $\mathbf{J}^{\mathrm{T}}\mathbf{v}$ is equivalent to running the forward modelling twice.